The influence of El Niño-Southern Oscillation on cool-season precipitation variability in the arid Middle East

Andries-Jan de Vries[1], Steven B. Feldstein[2], Jake W. Casselman[3], Georgios Fragkoulidis[4], Jos Lelieveld[5,6], Daniela I.V. Domeisen[1,7]

[1]Institute of Earth Surface Dynamics, University of Lausanne, Lausanne, Switzerland
[2]Department of Meteorology and Atmospheric Science, The Pennsylvania State University, University Park, PA, USA
[3]Department of Atmospheric Sciences, University of Hawaii, Mãnoa, USA
[4]Institute of Environmental Research and Sustainable Development, National Observatory of Athens, Athens, Greece
[5]Department of Atmospheric Chemistry, Max Planck Institute for Chemistry, Mainz, Germany
[6]Climate and Atmospheric Research Center (CARE-C), The Cyprus Institute, Nicosia, Cyprus
[7]Institute for Atmospheric and Climate Science, ETH Zürich, Zürich, Switzerland

Correspondence to: Andries-Jan de Vries (andries-jan.devries@unil.ch)

Abstract. Interannual variability in precipitation across the Middle East is of high societal and environmental relevance given the region's arid climate and limited water resources. While previous studies have linked the El Niño-Southern Oscillation (ENSO) to interannual precipitation variability in the Middle East, the understanding of this linkage and the underlying mechanisms remain fragmented. Using observation-based datasets and a range of diagnostics, this study quantifies the influence of ENSO on Middle Eastern precipitation variability during the extended cool season (October-May) and presents an integrated perspective on the driving atmospheric mechanisms. Consistent with previous studies, we find that El Niño is associated with increased precipitation, whereas La Niña is associated with decreased precipitation. This relationship is asymmetric and varies substantially within the cool season, with a strong precipitation increase during autumn and a modest increase in spring under El Niño conditions, and a persistent precipitation decrease throughout the cool season under La Niña conditions. These precipitation increases (decreases) during El Niño (La Niña) are associated with an equatorward (poleward) displacement of the subtropical jet and increased (decreased) Rossby wave breaking frequencies at the poleward flank and beneath the jet core. Simultaneously, a mid-tropospheric cyclonic (anticyclonic) circulation anomaly over the Middle East strengthens (weakens) atmospheric moisture transport into the region, contributing to enhanced (reduced) tropospheric moisture content and instability. From a global perspective, three different atmospheric mechanisms contribute to these regional circulation patterns: (1) a zonally symmetric shift in the meridional position of the subtropical jet along with anomalies in Rossby wave breaking frequency, (2) a barotropic Rossby wave response emanating from the tropical Pacific toward the Middle East via the extratropics, and (3) a baroclinic perturbation in the tropical circulation extending westwards over the Indian Ocean and South Asia consistent with a Gill-Matsuno-type response. Co-varying circulation patterns over the Indian Ocean, associated with the Indian Ocean Dipole, likely contribute to intraseasonal variability in ENSO's influence on Middle Eastern precipitation. Our findings advance process understanding of

precipitation variability in the water-scarce Middle East, having implications for seasonal prediction, flood and drought warning, and the evaluation of climate projections.

1 Introduction

The majority of the Middle East has an arid climate, making the region susceptible to water scarcity. Annual precipitation can reach up to 500 mm along the eastern Mediterranean coast and exceeds 1000 mm in parts of the Zagros Mountains and the Iranian Plateau but falls below 200 mm across most of the region, reaching as low as 20 mm in its hyper-arid deserts (Fig. 1b,c). Moreover, precipitation in the Middle East experiences strong interannual variability, making the region prone to both flooding and drought, which significantly impact society, the economy, agriculture, and ecosystems (Lelieveld et al. 2012; Barlow et al., 2016; Zittis et al. 2022; Coleman et al., 2026; Sohrabi, 2025). These hydrometeorological hazards can exacerbate geopolitical and social tensions in the region, while pre-existing tensions can make the population more vulnerable to such hazards. For example, the multi-year drought from 2007 to 2011 is believed to have acted as a catalyst for the Syrian uprising and civil war that began in 2011, as this drought caused widespread agricultural failure and displacement of over a million people in the region (Gleick, 2014; Kelley et al., 2015). The Libya flooding of September 2023, leaving more than 13,000 people dead or missing, was caused by heavy rainfall and the breaching of two dams, which were poorly maintained due to armed conflict and political dispute in the Derna region (Armon et al., 2025). Given the large impacts of precipitation deficits and surpluses on society and the environment, it is important to better understand the interannual variability of precipitation in the Middle East and the underlying drivers.

From a global perspective, the Middle East stands out as a region receiving most of its annual precipitation during the extended cool season. More than 95% of the annual rainfall occurs between October and May across a region stretching from Libya in the west to Pakistan in the east, and from the Zagros Mountains in the north to the central parts of the Arabian Peninsula in the south (Fig. 1a). During the hot summer months of June to September, the region remains almost entirely dry due to the influence of the South Asian monsoon, which induces strong subsidence over the eastern Mediterranean and Middle East (Rodwell and Hoskins, 1996, 2001; Tyrlis et al., 2013). During the transition seasons and in winter, the westerlies and subtropical jet migrate southward and can steer midlatitude weather systems into the region, contributing to most of the precipitation during these seasons. The midlatitude forcing typically manifests as extratropical Rossby waves propagating and breaking toward lower latitudes, whereby the associated upper-tropospheric cyclonic circulation anomalies interact with the tropical low-level circulation (Kahana et al., 2002; Kumar et al., 2015; De Vries et al., 2016, 2018). These tropical-extratropical interactions can direct warm, moist tropical air masses into the Middle East, supporting the development of convective storms and heavy precipitation.

Interannual variability of cool-season precipitation in the Middle East is strongly linked to the El Niño–Southern Oscillation (ENSO). The ENSO warm phase, El Niño, generally leads to an increase in precipitation over the Middle East, while its cold phase, La Niña, leads to a decrease. Previous studies have demonstrated this connection based on various types of observations, such as precipitation and river streamflow data in Iran, Israel, and Saudi Arabia (Kiladis and Diaz, 1989; Price et al., 1998; Nazemosadat and Cordery, 2000; Nazemosadat and Ghasemi, 2004; Athar, 2015; Saghafian et al., 2017), gridded precipitation datasets (Mariotti, 2007; Hoell et al., 2015a; Alizadeh and Mousavizadeh, 2025), climate model simulations (Kumar et al., 2016; Hoell et al., 2018, 2024), and seasonal predictions (Abid et al., 2016). The relationship between ENSO and precipitation in the Middle East is not constant over time but varies on interdecadal scales and within the cool season. While El Niño has been associated with a consistent precipitation increase throughout the 20th century, the link between La Niña and reduced precipitation becomes apparent only from the 1970s onward (Price et al., 1998; Kang et al., 2015; Hoell et al., 2017; Dasari et al., 2021). Although precipitation tends to increase during El Niño and to decrease during La Niña, several studies suggested that the strength of this linkage varies during the wet season, with the strongest influence during autumn, a weak influence during winter, and a modest influence in spring (Mariotti et al., 2005; Mariotti, 2007; Bahrami et al., 2021; Hochmann et al., 2024; Alizadeh and Mousavizadeh, 2025; Nuroozi et al., 2025).

Previous studies have suggested various mechanisms by which forcing in tropical Pacific Sea surface temperatures (SSTs) can modulate precipitation variability over the remote Middle East (Barlow et al., 2016). Anomalies in tropical convection, linked to SST variability in the tropical central Pacific, generate a barotropic Rossby wave train that propagates eastward from the Pacific towards the Middle East via the extratropics (Kumar et al., 2016; Hoell et al., 2013b; Hoell et al., 2015a; Abid et al., 2020). During El Niño, these circulation patterns are accompanied by a cyclonic anomaly over the Middle East, enhancing precipitation through the advection of warm, moist air and large-scale ascent (Chakraborty et al., 2006; Mariotti, 2007; Hoell et al., 2018). Conversely, during La Niña, an anticyclonic circulation anomaly emerges over the region, reducing precipitation through cold air advection, weakened moisture transport, and large-scale descent (Abid et al., 2016; Hoell et al., 2014a, 2014b, 2018). Furthermore, El Niño conditions are associated with an equatorward shift of the subtropical jet over North Africa and the Middle East, leading to increased westerly winds and storm activity over the region, and thereby increasing precipitation (Kumar et al., 2016; Alizadeh-Choobari et al., 2018; Sandeep and Ajayamohan, 2018; Hoell et al., 2024). Conversely, under La Niña conditions, a poleward displacement of the subtropical jet leads to decreased westerly winds, storms, and precipitation. Other studies have suggested that tropical convection anomalies over the Indo-Pacific modify the tropical circulation through a Rossby wave response in the form of an upper-tropospheric warm structure extending northwestward toward the Middle East region, consistent with the Gill-Matsuno model (Barlow et al., 2002; Hoell et al., 2012; Hoell et al., 2015a, 2018). In summary, previous studies have suggested that Indo-Pacific SST variability can influence Middle East precipitation through three atmospheric pathways: a barotropic Rossby wave response moving eastward via the midlatitudes, a meridional displacement of the subtropical jet, and a baroclinic response in the tropical circulation to tropical convection extending westward in the form of a Gill-Matsuno gyre.

Previous work has also identified an influence of Indian Ocean SSTs on Middle East precipitation. Variability in Indian Ocean SSTs is often expressed by the Indian Ocean Dipole, with positive SST anomalies in the west and negative anomalies in the east during its positive phase, and vice versa during its negative phase (Saji et al., 1999). Over the past four decades, the positive (negative) phase of the Indian Ocean Dipole has been associated with enhanced (reduced) precipitation across the Middle East (Athar et al., 2015; Pourasghar et al., 2019; Tuel et al., 2022; Hochman et al., 2024). Moreover, it has been argued that El Niño (La Niña) events co-occurring with a positive (negative) Indian Ocean Dipole have an amplifying effect on precipitation anomalies (Chakraborty et al., 2006; Abid et al., 2020; Hochman and Gildor, 2024; Hoell et al., 2025). It is important to note that ENSO and the Indian Ocean Dipole are interconnected, but that they exhibit different seasonality. El Niño tends to coincide with the positive phase of the Indian Ocean Dipole, while La Niña aligns with its negative phase (Schott et al., 2009; Stuecker et al., 2017). ENSO usually peaks during boreal winter, whereas the Indian Ocean Dipole is mainly active during boreal summer and autumn (Schott et al., 2009). This suggests that the Indian Ocean basin can act as a pathway through which ENSO influences precipitation variability in the Middle East during specific seasons (Abid et al., 2020).

While the relationship between ENSO and Middle East precipitation variability has been widely investigated, previous studies tend to focus on (1) cool season averages or single seasons only, (2) specific areas or countries within the broader Middle East, (3) correlation with indices that represent ENSO variability without accounting for the asymmetric influences of ENSO warm and cold phases, and (4) only one of the mechanistic pathways through which ENSO can modulate Middle East precipitation variability. This study presents an integrated perspective on the influence of ENSO on Middle East precipitation variability at local and spatially aggregated scales during the cool-season and its individual months. Furthermore, this study explores the atmospheric processes through which ENSO shapes precipitation variability in the Middle East by quantifying anomalies in large-scale circulation patterns and synoptic-scale weather systems. Specifically, we extend previous studies by diagnosing the latitudinal position of the subtropical jet stream and its linkage with Rossby wave breaking and by quantifying thermodynamic characteristics of the atmosphere such as atmospheric moisture content and transport and tropospheric instability. Finally, we synthesize various mechanisms by which tropical Pacific SST variability shapes regional circulation patterns and hydroclimatic conditions over the Middle East.

This study is structured as follows. Section 2 details the methodology, diagnostics, and data used. Section 3 quantifies the influence of the warm, neutral, and cold ENSO phases on Middle East precipitation variability at local and regional scales and during the extended cool season and its individual months. Section 4 explores the influence of ENSO on the subtropical jet and extratropical Rossby wave breaking. Section 5 examines the effect of ENSO on tropospheric moisture and instability over the Middle East. Section 6 discusses different mechanisms and pathways from a global perspective. Finally, section 7 summarizes the main findings and limitations of the study.

2. Data and methodology

2.1 ENSO events and tropical Pacific SST variability

To quantify tropical Pacific SST variability, we compute the Oceanic Niño Index (ONI) using monthly SSTs from the Extended Reconstructed Sea Surface Temperature dataset version 6 (ERSSTv6; Huang et al., 2025a, 2025b). We compute SST anomalies in the Nino3.4 region (5°S to 5°N, 120°W to 170°W) using linearly detrended timeseries over the period of 1979-2024. For defining ENSO phases during the cool season, we use the Nino3.4 index based on 5-monthly running mean SST anomalies from October to February. Warm, neutral, and cold ENSO phases are then defined by values ≥ 0.5°C, ≥ —0.5°C and < 0.5°C, and < —0.5°C, respectively (cf. Casselman et al., 2021). Similarly, we define tropical Pacific SST variability for the analysis at monthly timescales by using the Nino3.4 index based on 3-monthly running mean SST anomalies to account for intraseasonal variability in tropical Pacific SSTs, having particular relevance for autumn and spring months.

2.2 Precipitation data and region of interest

Precipitation observations covering the Middle East region are subject to limitations in data quality and availability. Measurements from in-situ stations often have missing data and limited spatial coverage, particularly over less populated areas and they are often not publicly available. Satellite-based measurements offer high spatial and temporal resolution but may be of lower quality in regions without station data, which are used to adjust satellite estimates. Moreover, satellite data generally span relatively short periods starting in 1998, which severely reduces the sample size of ENSO events available for analysis. Reanalysis precipitation data are physically consistent and provide full spatial and temporal coverage but are derived from short-range numerical model forecasts. For these reasons, we use the Multi-Source Weighted Ensemble Precipitation (MSWEP) version V280 for the period 1979–2020 (Beck et al., 2019). This dataset combines precipitation estimates from reanalysis, stations, and satellites to leverage the respective strengths of each data source.

To quantify the influence of tropical Pacific SST variability on spatially aggregated precipitation and atmospheric conditions over the arid Middle East, we define a target region within 10-70°E and 10-45°N. We define our target region based on three criteria, that is, grid points (1) receiving more than 95% of their annual precipitation totals during the extended cool season, lasting from October to May, (2) having an arid to hyper-arid climate, defined by the aridity index (Middleton and Thomas, 1997) – the ratio of precipitation to potential evapotranspiration – falling below 0.2 in monthly data from the Climate Research Unit (CRU; Haris et al., 2020), and (3) covering land area only, based on the ERA5 land sea mask with values equal or larger than 0.5. These three criteria are demonstrated by the contour lines in Fig. 1. Note that our region of interest extends somewhat beyond the area typically defined as the Middle East and covers a substantial portion of Southwest Asia. Nevertheless, following common practice, we use the term Middle East throughout this study when referring to the region of interest.

2.3 Precipitation and dry-day events

To provide a reference for interpreting how ENSO shapes the atmospheric circulation modulating precipitation variability in the Middle East, we construct atmospheric circulation composites based on precipitation and dry-day events. To this end, we compute time series of daily precipitation aggregated over the target region as described in section 2.2. Precipitation events are defined by at least two consecutive days with spatially aggregated precipitation amounts that exceed the 21-day running mean climatology by 100% (i.e., a doubling). Likewise, dry-day events are defined by at least two consecutive days with daily spatially aggregated precipitation falling 90% below climatology (i.e., less than 10% of the climatological precipitation). Note that, while dry conditions are very common in the Middle East at the local scale, dry-day events are here based on spatially aggregated precipitation over a very large area. The 21-day running mean is used to account for the strong seasonal cycle of precipitation. While the chosen thresholds of 100% and -90% are somewhat arbitrary, they give approximately similar sample sizes of precipitation events (n = 377) and dry-day events (n = 394).

2.4 Atmospheric reanalysis and diagnostics

To determine the large-scale atmospheric circulation and synoptic-scale processes through which ENSO modulates precipitation variability in the Middle East, we use ERA5 reanalysis data (Hersbach et al., 2020) of the European Centre for Medium-Range Weather Forecasts (ECWMF). The ERA5 reanalysis provides a global reconstruction of past weather by combining numerical model simulations with a wide range of observations. We linearly detrend cool season and monthly mean data for the period of 1979-2020 to remove the influence of trends and to focus on interannual variability. We estimate the significance of anomalies in spatial fields and spatially aggregated values for ENSO phases relative to climatology by using a Monte Carlo test with 10,000 randomly drawn samples of cool season or monthly means during the reference period. The Monte Carlo simulations are used to construct a random distribution for testing the significance of observed values by applying a two-sided test at the $p < 0.05$ level, unless otherwise specified.

We use several diagnostics to characterize the large-scale circulation patterns, synoptic-scale processes, and the thermodynamic state of the atmosphere under different ENSO conditions. The latitudinal position of the jet axis is derived from the zonal mean (20-60°E) 250-hPa zonal wind maxima across the latitude range of 18-44°N in a similar fashion as in Hart et al. (2018). This relatively simple measure provides an estimate of the meridional position of the jet axis over the North Africa and Middle East region during the cool-season average and in individual months.

We also use a diagnostic for identifying Rossby wave breaking given that previous studies linked this atmospheric process to precipitation in arid subtropical regions, including the Middle East (De Vries et al., 2018, 2024; De Vries, 2021). Rossby wave breaking is defined by elongated and separated structures of stratospheric air masses at the dynamical tropopause with potential vorticity (PV) values > 2 PV units (PVU; 1 PVU = $1*10^{-6}$ kg K^{-1} m^2 s^{-1}), so-called PV streamers and cutoff lows

(Wernli and Sprenger, 2007). More specifically, we use 2 PVU contours on isentropic surfaces between 275 and 360 K with 5 K intervals at 6-h timesteps. PV streamers are defined by geometric criteria and PV cutoff lows are tested for stratospheric origin by applying thresholds on absolute and relative humidity to remove diabatic structures. Hereafter, these objectively identified PV streamers and cutoff lows are referred to as stratospheric PV structures. For more details on the methodology, we refer to De Vries et al. (2024).

Finally, we quantify atmospheric moisture content and atmospheric moisture transport by using vertically integrated water content, i.e., total column water (TCW), and vertically integrated horizontal water vapor transport (IVT), both directly available in ERA5. Furthermore, we use a proxy of tropospheric instability based on vertical profiles of moist static energy, similar to Hart et al. (2018). More specifically, we compute moist static energy (h), defined by the sum of internal, latent heat, and potential energy:

$$h = C_p T + L_v q + \phi \qquad (1)$$

where C_p is the specific heat at constant pressure, T is air temperature, L_v is the latent heat of vaporization, q is specific humidity, and ϕ is geopotential. We consider vertical profiles of moist static energy in monthly mean data whereby a decreasing h with height (dh/dp > 0) represents a conditionally unstable layer. To diagnose tropospheric instability (I_{max}) within a given vertical profile, we vertically integrate the mass-weighted difference between h_{bot} and $h(p)$ from a given pressure level (p_{bot}) to the pressure level p_{top}, where p_{top} corresponds to the pressure level that yields the largest value of the integral:

$$I_{max} = g^{-1} \int_{p_{top}}^{p_{bot}} (h_{bot} - h(p))\, dp \qquad (2)$$

where g is gravitational acceleration. To compute the maximum value I_{max} within a given vertical profile, we repeat this computation by taking different pressure levels for p_{bot} and integrating over pressure levels upward. In this sense, I_{max} is analogue to most unstable convective available potential energy (CAPE) but is based on the moist stratification of tropospheric layers instead of a parcel-based perspective, and is therefore less sensitive to the relatively coarse vertical resolution of reanalysis data. I_{max} provides an estimate of the susceptibility of the tropospheric environment for developing deep moist convection and includes the effects of deep convection on this environment. This quantity is typically very large in the tropics and low in midlatitudes and thus provides a helpful measure to diagnose the influence of warm, moist tropical air masses on Middle Eastern precipitation variability.

3. Precipitation variability

Figure 2 presents the spatial distribution, time evolution, and statistical relationship between cool-season Middle Eastern precipitation and ENSO as represented by the Nino3.4 index. Consistent with the consensus in the literature, we observe an increase in precipitation during El Niño and a decrease during La Niña. During El Niño events, precipitation exhibits a weak but significant increase over parts of the Middle East, exceeding 10% and locally reaching up to 20% above climatology (Fig. 2a). In contrast, La Niña events show a moderate and significant decrease in precipitation falling below 20% of climatology across much of the region and decreasing by more than 35% over the Sinai Peninsula, the southern parts of the Arabian Peninsula, and the southern coasts of Iran and Pakistan (Fig. 2c). During the neutral ENSO phase, precipitation does not deviate significantly from climatology apart from the northern part of the Red Sea and surrounding land areas, where precipitation increases by up to 35% (Fig. 2b).

Consistent with the spatial distribution, the timeseries of spatially aggregated cool-season precipitation generally show positive anomalies during El Niño events and negative anomalies during La Niña events (Fig. 2d). Particularly striking are the multi-year La Niña events during 1998/1999-2000/2001 and 2007/2008-2011/2012, both of which were associated with severe drought (Barlow et al., 2002; Hoell et al., 2014a). The timeseries also indicate some atypical seasons, such as a decrease in precipitation during the El-Niño seasons of 1986/1988, 2002/2003, 2009/2010, and 2014/2015, and an increase in precipitation during the La Niña seasons of 1984/1985 and 1995/1996. These deviations from the commonly observed ENSO – Middle East precipitation patterns have previously been linked to variations in SST gradients between the western and central Pacific and to the extension of Pacific SST anomalies into the eastern Indian Ocean (Hoell et al., 2013a, 2014b). The timeseries also hint at interdecadal variability in Middle East precipitation, typically showing wet conditions during the period from 1979 to 1998, followed by two decades of dry conditions from 1999 to 2017. Earlier studies have suggested a linkage with multi-decadal variability in both the Pacific and Atlantic Oceans (Kang et al., 2015; Hoell et al., 2015b; Dasari et al., 2021; Rezaei, 2023; Saharwardi et al., 2024), although their respective contributions and underlying mechanisms remain unclear.

The statistical distribution of spatially aggregated precipitation differs substantially among ENSO warm, neutral, and cold phases (Fig. 2e). Relative to climatology, the spatially aggregated mean precipitation is significantly higher during El Niño and significantly lower during La Niña. Consistent with these differences between ENSO warm and cold phases, the interquartile range of precipitation during El Niño lies entirely above the interquartile range of precipitation during La Niña (red and blue boxes in Fig. 2e). Additionally, the relationship between cool-season precipitation and ENSO exhibits substantial asymmetry (Fig. 2e,f). Mean anomalies in spatially aggregated precipitation from the multi-year mean (99.3) are substantially larger during La Niña (-19 mm) than during El Nino (+14 mm; Fig. 2e). Linear regression of cool-season precipitation as a function of the Nino3.4 index shows a change in precipitation per degree of central Pacific SST anomalies (i.e., the slope) of approximately 25.5 mm °C^{-1} and 9.1 mm °C^{-1} for Nino3.4 index values below −0.5 and above 0.5, respectively, a nearly threefold difference (Fig. 2f). The slope in precipitation to ENSO forcing is significant for Nino3.4 index values below −0.5 with a $p\text{-}value < 0.11$ and non-significant for Nino3.4 index values above 0.5 ($p\text{-}value = 0.41$). The Pearson correlation between the Nino3.4 index and spatially aggregated precipitation amounts is 0.44 and 0.24 for Nino3.4 index values below −0.5 and above 0.5, respectively. These computations demonstrate that the Middle Eastern precipitation response to ENSO forcing is stronger for La Niña than for El Niño.

On monthly timescales, Middle East precipitation shows a similar relationship with ENSO as in the cool-season average, albeit with some inter-monthly variations (Figs. 3 and A1). During El Niño conditions, the spatially aggregated precipitation increases substantially during autumn and modestly during spring compared with neutral ENSO and La Niña conditions (Fig. 3a). The spatially aggregated precipitation average is more than doubled in October and approximately one-and-a-half times larger in November compared with neutral ENSO conditions. In the spring months (March, April, and May), precipitation also enhances under El Niño conditions compared with neutral ENSO conditions with a significant increase in the spatially aggregated mean for the month of May only. Note that the precipitation increase under El Niño conditions is not only apparent from the mean, but also from the precipitation distribution in general, showing substantial increases for the 25th, 50th, and 75th percentiles (Fig. 3a). Conversely, La Niña conditions consistently exhibit a substantial reduction in precipitation compared with El Niño and neutral ENSO conditions throughout the cool season with significant decreases in the spatially aggregated mean during October, December, March and May at the $p < 0.05$ level and for November and April at the $p < 0.1$ level (Fig. 3c). During the core winter months of January and February, precipitation tends to be higher under neutral ENSO conditions compared to both El Niño and La Niña conditions, with a significant increase in the spatially aggregated mean for the month of January at $p < 0.1$ (Fig. 3b). Consistent with this notion, Hoell et al. (2015a) documented different correlation patterns of hydroclimate conditions over Southwest Asia with tropical Pacific SST anomalies for the month of January compared with other cool-season months.

In summary, our findings show that ENSO has an asymmetric influence on Middle East precipitation with a stronger decrease during La Niña and a somewhat milder increase during El Niño (cf. Hoell et al., 2018). This relationship varies strongly within the cool season with, under El Niño, the largest precipitation increases during autumn (cf. Mariotti et al., 2005; Mariotti, 2007; Bahrami et al., 2021; Hochmann et al., 2024; Alizadeh and Mousavizadeh, 2025) and modest increases during spring, contrasting with a persistent precipitation decrease under La Nina conditions throughout the cool season. The asymmetric influence and intraseasonal variations are largely missed when considering cool-season averages or simple correlations with ENSO indices, and thus must be considered when assessing ENSO-related precipitation variability and predicting hydrometeorological hazards in the region. Note that the influence of ENSO on Middle Eastern precipitation variability is susceptible to decadal variability, and thus, does not ensure a similar relationship before and after our period of consideration nor a stationary relationship during our period of consideration (1979-2020).

4. Midlatitude dynamical forcing: the subtropical jet and Rossby wave breaking

Midlatitude forcing plays a key role in the formation of precipitation across the Middle East during the cool season. Extratropical Rossby waves propagate and break towards lower latitudes, resulting in the formation of upper-level troughs and often cut-off lows (Kahana et al., 2002; Kumar et al., 2015; De Vries et al., 2016, 2018; Tuel et al., 2022; Francis et al., 2025). These upper-level cyclonic circulation patterns can induce cyclogenesis near the surface, intense atmospheric moisture transport from southerly directions, and large-scale ascent, leading to tropospheric conditions conducive to the occurrence of deep moist convection. In this section, we analyze the anomalies in the subtropical jet and Rossby wave breaking occurrences during precipitation and dry-day events at daily timescales to provide a reference for interpreting similar anomalies during ENSO warm and cold phases at seasonal to monthly timescales.

Figure 4 shows anomalies in zonal wind and relative anomalies in Rossby wave breaking frequencies based on precipitation and dry-day events in the Middle East. Rossby wave breaking frequencies are here defined by the counts of stratospheric PV structures summed across isentropic surfaces from 300 to 350K with 5K intervals. Anomalies in zonal winds demonstrate that precipitation events are accompanied by increased zonal winds at the equatorward flank of the subtropical jet over North Africa and the Middle East and decreased zonal winds at its poleward flank, suggesting an equatorward shift of the subtropical jet (Fig. 4a,b). Rossby wave breaking frequencies more than double, evident from relative anomalies in stratospheric PV structure frequencies exceeding 100% above climatology, primarily on the poleward flank of the subtropical jet (between 20-33°N) and beneath the jet core (between 800 and 200 hPa), confirming the central role of Rossby wave breaking in Middle Eastern precipitation (Fig. 4a,b). In contrast, during dry-day events, the subtropical jet shifts poleward and Rossby wave breaking frequencies decrease at the poleward edge and beneath the subtropical jet (Fig. 4c,d). The southwest-northeasterly orientation of PV structure frequency anomalies during both precipitation and dry-day events is suggestive of anticyclonic Rossby wave breaking imposing an upper-tropospheric trough and ridge over the region during wet and dry conditions, respectively. Furthermore, during both precipitation and dry-day events, anomalies in PV structure frequencies of opposite sign emerge farther upstream and downstream of the largest anomalies over the eastern Mediterranean, reflecting the typical structure of Rossby wave packets with multiple neighboring troughs and ridges embedded within wave packets.

Consistent with previous studies (Kumar et al., 2016; Alizadeh-Choobari et al., 2018; Sandeep and Ajayamohan, 2018), Figure 5 shows that El Niño conditions are associated with an equatorward shift of the subtropical jet, whereas La Niña conditions are associated with a poleward shift of the jet. During El Niño events, positive zonal wind anomalies appear on the equatorward flank of the jet, peaking above its core near 150 hPa, while negative zonal wind anomalies occur on the poleward flank of the jet (Fig. 5a,b). These changes in the background zonal wind go along with increased frequencies in stratospheric PV structures exceeding 10% on the poleward flank and beneath the subtropical jet core (Fig. 5a,b). Conversely, La Niña events demonstrate opposite patterns with negative zonal wind anomalies on the equatorward side and positive anomalies on the poleward side of the jet, going along with a reduction of more than 10% in stratospheric PV structure frequencies poleward and beneath the subtropical jet (Fig. 5c,d). In essence, composites of anomalies in the subtropical jet and Rossby wave breaking occurrences during ENSO warm and cold phases resemble the patterns observed during precipitation and dry-day events. This suggests that El Niño events bring about wet conditions through an equatorward displacement of the subtropical jet accompanied by increased Rossby wave breaking occurrences, while La Niña events exhibit dry conditions linked to a poleward displaced jet associated with decreased Rossby wave breaking occurrences. Figure 5 also shows anomalies in stratospheric PV structure frequencies with opposite sign at the equatorward flank of the subtropical jet (between 10-20°N), that is, negative anomalies during El Niño and positive anomalies during La Niña. However, given that these anomalies arise outside regions of stratospheric PV structure imprints during precipitation and dry-day events, shown by purple and green contours in Fig. 5, respectively, we consider these anomalies irrelevant for understanding precipitation anomalies during ENSO warm and cold phases.

On monthly timescales, similar patterns emerge as during the cool season average, displaying an equatorward (poleward) displacement of the subtropical jet during El Niño (La Niña) conditions (Figs. A2, A3). Increased (decreased) Rossby wave breaking occurs beneath and poleward of the subtropical jet during El Niño (La Niña) conditions, primarily during October, November, and December and to a lesser extent in March and May. To further quantify the relationship between ENSO and the large-scale circulation over the Middle East, we evaluate the distribution of the latitudinal position of the jet stream during each month and ENSO phase (Fig. 6). The multi-year monthly mean jet position during different ENSO phases, depicted by the dots, generally aligns with the monthly distribution of anomalies in precipitation and Rossby wave breaking occurrences. Under El Niño conditions, the jet is displaced southward in October ($p < 0.05$), November ($p < 0.1$), December and April (non-significant) compared with neutral ENSO conditions (Fig. 6a), consistent with increased precipitation and wave breaking frequencies during these months (Figs. 3a, A2, A3). Under La Niña conditions, the jet is displaced poleward in January, February, and May ($p < 0.05$) and in November and March (non-significant), compared with neutral ENSO conditions (Fig. 6c), consistent with decreased precipitation and wave breaking frequencies during these months (Figs. 3c, A2, A3). Some months deviate from these patterns, showing jet displacements that are inconsistent with anomalies in precipitation and/or Rossby wave breaking frequencies. For example, under El Niño conditions, the jet shows a significant southward displacement in February (Fig. 6a), which contrasts with the non-significant precipitation decrease during that month relative to neutral ENSO conditions (Fig. 3a). Similarly, under La Niña conditions, the mean jet position in December is very similar to that under neutral ENSO conditions (Fig. 6c), despite the significant decrease in precipitation and Rossby wave breaking frequencies compared with neutral ENSO conditions during this month (Figs. 3c, A2, and A3).

In summary, apart from some deviations in specific months, the atmospheric circulation composites generally show that El Niño conditions are associated with a southward displaced jet and increased wave breaking frequencies at its poleward flank and beneath its core, while La Niña conditions are associated with a poleward displaced jet and decreased wave breaking frequencies. The similarity between the ENSO-based composites and those based on precipitation and dry-day events suggests that El Niño and La Niña events induce wet and dry conditions, respectively, through latitudinal shifts in the jet stream accompanied by anomalies in Rossby wave breaking frequencies.

5. Thermodynamic considerations: tropospheric moisture and instability

Precipitation in the Middle East is associated with intrusions of warm and moist air masses from southerly directions that support the formation of deep moist convection. Previous studies have shown that ENSO variability is linked to anomalies in atmospheric moisture content and transport over the Middle East (Chakraborty et al., 2006; Mariotti et al., 2005, Mariotti, 2007; Hochman and Gildor, 2024). Consistent with these findings, Fig. 7a shows increased atmospheric moisture content and strengthened moisture transport from southwesterly directions during El Niño conditions. It is important to note that climatological moisture transport over the Middle East is primarily from southwesterly directions (not shown). Conversely, under La Niña conditions, atmospheric moisture content decreases, and anomalies in atmospheric moisture transport have northeasterly directions, suggesting reduced moisture transport into the region (Fig. 7c). These anomalies emerge at the southeastern flanks of mid-tropospheric cyclonic and anticyclonic circulation anomalies, pointing to ENSO forcing on midlatitude circulation patterns through which El Niño and La Niña conditions strengthen and weaken moisture transport into the Middle East, respectively. The alignment of anomalous IVT vectors with 500-hPa geopotential height anomaly contours suggests a barotropic Rossby wave response to tropical Pacific SST forcing. However, farther southeast from the region of interest, anomalous IVT vectors display an approximately perpendicular or even opposing alignment with 500-hPa geopotential height anomalies, suggesting a baroclinic response of tropospheric circulation to ENSO variability. We will return to this aspect in section 6.

On monthly timescales, anomalies in atmospheric moisture content and transport show patterns very similar to the cool season average (Fig. A4), while monthly variations in these patterns align with the monthly precipitation anomalies (Fig. A1). Spatially aggregated total column water content follows a strong seasonal cycle with the highest values in summer and the lowest values during winter (Fig. 8). Despite the greatest availability of moisture in summer, the region remains dry due to large-scale subsidence over the broader Middle East, which suppresses upward motion (Tyrlis et al., 2013). During autumn, westerly winds and the subtropical jet migrate southward, along with the decay of the South Asian summer monsoon circulation, allowing extratropical disturbances to reach the region. The availability of both dynamically forced ascent and atmospheric moisture during the transition seasons and in winter facilitates the occurrence of precipitation during this period of the year. Spatially aggregated mean values of atmospheric moisture content show a significant increase under

El Niño conditions during October ($p < 0.05$), November ($p < 0.1$), and May ($p < 0.05$) (Fig. 8a). Conversely, La Niña conditions show decreases during all cool season months compared with neutral ENSO condition with significant departures from climatology ($p < 0.05$) during October-December and March-May (Fig. 8c). In January, moisture content is significantly increased for neutral ENSO conditions (Fig. 8b), consistent with the precipitation increase during that month and ENSO phase (Fig. 3b).

To provide a complementary perspective on how ENSO shapes a tropospheric environment conducive to deep moist convection, we evaluate the spatial distribution and spatially aggregated mean values of tropospheric instability. During the cool season, I_{max} exhibits patterns similar to those in TCW with significant positive anomalies across the Middle East during El Niño and significant negative anomalies during La Niña (Fig. 9). Anomalies are particularly large over the Arabian Peninsula and along the southern flanks of the Zagros Mountains. Anomalies of opposite sign emerge over the Red Sea and Persian Gulf, that is, negative anomalies during El Niño and positive anomalies during La Niña, most likely resulting from weak negative and positive SST anomalies over these waters during El Niño and La Niña conditions, respectively (not shown). On monthly timescales, I_{max} shows a strong seasonal cycle with the largest values during summer and the lowest values during winter (Fig. 10). Monthly anomalies in I_{max} for ENSO conditions follow anomalies in TCW and precipitation (Fig. A5). Under El Niño conditions, spatially aggregated mean values of I_{max} show positive anomalies during October, November, December and April being significant ($p < 0.05$) for October only (Fig. 10a). During La Niña conditions, negative anomalies persist throughout all cool season months with significant departures from climatology in October and May at $p < 0.05$ and March and April at $p < 0.1$ (Fig. 10c).

6. A global perspective on ENSO mechanisms modulating Middle Eastern precipitation variability

We now have a clearer understanding of how precipitation and regional circulation patterns over the Middle East relate to ENSO. Still, the question remains how remote SST forcing in the tropical Indo-Pacific brings about these changes in atmospheric circulation and surface weather over a region on the opposite side of the globe. As articulated in the introduction, previous studies have proposed various mechanisms and pathways through which ENSO influences the hydroclimate of the Middle East (Barlow et al., 2016). Here we argue, based on physical reasoning and global composites, that all three previously proposed atmospheric mechanisms hold validity, and that co-varying atmosphere-ocean interactions over the Indian Ocean are likely responsible for the seasonally varying influence of ENSO on Middle Eastern precipitation.

Seager et al. (2003, 2005) have shown that hemispheric symmetric variability in precipitation at interannual timescales can be attributed to ENSO (see also Fig. 11a, d). During El Niño conditions, increased heating of the tropical atmosphere is associated with an equatorward shift and strengthening of the subtropical jet in the global zonal mean along with increased baroclinicity at lower latitudes (Seager et al., 2003). While their focus was primarily on the eastward extension of the subtropical jet over the East Pacific, leading to a regional increase in precipitation over the West Coast of North America and the southern United States (Seager et al., 2005), the equatorward shift in the subtropical jet also manifests over North Africa, the Middle East, and South Asia (Fig. 11c). This equatorward shift goes along with increased Rossby wave breaking frequencies on the poleward flank of the jet over northwest Africa, the Middle East, and southwest and central South Asia. This notion is consistent with previous studies reporting an equatorward shift of the subtropical jet and increased (extreme) precipitation at the western flanks of the Himalayas (Cannon et al., 2017; Bharati et al., 2025; Hunt et al., 2025). Conversely, during La Niña conditions, zonal winds weaken at the southern flank of the subtropical jet and strengthen at its poleward side across a region spanning from the East Atlantic through North Africa, the Middle East, South Asia, and reaching the west Pacific coast (Fig. 11f). Rossby wave breaking occurrences are significantly reduced along the entire poleward flank of the subtropical jet. Therefore, ENSO forcing induces a zonally symmetric response in the circulation, manifesting as a meridional shift of the subtropical jet and modifications in Rossby wave breaking frequencies at its poleward flank, bringing about precipitation anomalies across a larger region encompassing the Middle East and southwest and central Asia (Fig. 11a,d).

Seager et al. (2005) also recognized a zonally asymmetric component of the precipitation response to ENSO, which is generally explained by a Rossby wave response to anomalous tropical Pacific SSTs and convection (Wallace and Gutzler, 1981; Hoskins and Ambrizzi et al., 1993). These stationary Rossby wave patterns emanate from the tropical central Pacific and arch in an eastward direction across North America, the North Atlantic, and reach North Africa and Europe (Fig. 11b,e). During El Niño events, this Rossby wave response appears as an anticyclonic anomaly over northwest Africa and southwestern Europe and a cyclonic anomaly over the Middle East (Fig. 11b), offsetting and strengthening the precipitation response to the zonally symmetric shift of the jet stream and wave breaking anomalies, respectively. During La Niña events, the signs of these anomalies reverse, with cyclonic and anticyclonic circulation patterns over northwest Africa-southwestern Europe and the Middle East, respectively (Fig. 11e). These patterns correspond to previously documented responses of the atmospheric circulation to tropical convection anomalies in the Indo-Pacific at interannual timescales, manifesting as an equivalent barotropic Rossby wave response derived from their consistent vertical structure (Hoell et al., 2012, 2013b, 2015a; Kumar et al., 2016). Additionally, several studies have also identified a baroclinic response in the tropical circulation over the Indian Ocean – South Asia sector to tropical convection anomalies over the Warm Pool, taking the form of a Gill-Matsuno-gyre (Barlow et al., 2002; Hoell et al., 2012; Hoell et al., 2015a). The Gill-Matsuno response explains that anomalous tropical heating (cooling) leads to a Rossby wave response, interacting with the mean flow, in the form of an upper-tropospheric anticyclonic (cyclonic) circulation anomaly to the northwest and southwest, accompanied by a lower-tropospheric cyclonic (anticyclonic) circulation anomaly (Matsuno, 1966; Gill, 1980). Accordingly, Fig. 11b shows an upper-tropospheric cyclonic circulation anomaly centered over southeast Asia (100°E and 30°N) to the northwest of reduced tropical convection over the Warm Pool. This cyclone extends westward across South Asia and the Middle East. In the lower troposphere, an anticyclonic circulation anomaly is evident based on the clockwise orientation of anomalous atmospheric moisture transport over the Indian Ocean and South Asia, including anomalous southwesterly IVT over the Middle East, implying strengthened atmospheric moisture transport into the region. The reversed pattern manifests during La Niña, with an upper-troposphere anticyclonic anomaly emerging over southeast Asia to the northwest of enhanced tropical convection over the Warm Pool. This circulation anomaly extends westward across South Asia and the Middle East, accompanied by an anomalous counterclockwise circulation in the lower troposphere, setting up anomalous northeasterly moisture transport over the Middle East, and thus reducing moisture transport into the region (Fig. 11e). The circulation response over the Middle East to Indo-Pacific tropical convection anomalies is consistent with the monsoon-desert mechanism of Rodwell and Hoskins (1996, 2001). According to this mechanism, reduced (enhanced) tropical convection sets up west-to-east upsloping (down sloping) isentropic surfaces facilitating isentropic upward-moving (down-gliding) air masses, resulting in large-scale ascent (subsidence), favoring (suppressing) precipitation formation (Barlow et al., 2005, 2007). This mechanism is evident from widespread mid-tropospheric ascent (descent) over the broader Middle East region in Fig. 9a (Fig. 9c).

To summarize, bringing together the findings from previous research and supported by composites in Fig. 11, we postulate that ENSO modulates precipitation variability in the Middle East through a combination of at least three distinct atmospheric pathways (Fig. 13): (1) a zonally symmetric latitudinal shift in the subtropical jet stream (Kumar et al., 2016; Alizadeh-Choobari et al., 2018; Sandeep and Ajayamohan, 2018; Hoell et al., 2024) alongside changes in Rossby wave breaking occurrences at its poleward flank, (2) a barotropic Rossby wave pattern arching from the central tropical Pacific eastward across North America, the Atlantic, and the European – North Africa region (Kumar et al., 2016; Hoell et al., 2013b; Hoell et al., 2015a; Abid et al., 2020), and (3) a baroclinic response in the tropical circulation extending westwards from the Warm Pool across the Indian Ocean-South Asia sector into the Middle East, consistent with a Gill-Matsuno-type response (Barlow et al., 2002; Hoell et al., 2012; Hoell et al., 2015a). While these mechanisms contribute to precipitation anomalies during the cool season, the inter-monthly variations of precipitation to ENSO forcing remain enigmatic. To investigate this aspect further, we focus our attention on the co-varying state of the atmosphere over the Indian Ocean.

Figure 11b,e not only shows outgoing longwave radiation anomalies over the central and western Pacific, but also over the western Indian Ocean. To further explore this signal, we construct Hovmöller diagrams of anomalies in monthly mean outgoing longwave radiation across the equator as a function of longitude and season under El Niño and La Niña conditions (Fig. 12). Besides the expected dipole in tropical convection over the central and western Pacific, which persists throughout the year, we also notice a seasonally asymmetric response in tropical convection over the western Indian Ocean. Specifically, under El Niño conditions, we observe significantly increased tropical convection over the western Indian Ocean (40-70°E) from October to December and weak anomalies of the same sign in May. Conversely, under La Niña conditions, tropical convection decreases significantly over the western Indian Ocean from October to December and again in April and May. In essence, ENSO-driven tropical convection anomalies over the western Indian Ocean follow the same pattern as the seasonally varying and asymmetric response of precipitation in the Middle East to ENSO (Fig. 3). This suggests that ENSO, beyond the three atmospheric pathways, also influences the Middle East hydroclimate through its effect on the Indian Ocean and atmospheric state (cf. Abid et al., 2020; Hochman and Gildor, 2024).

7. Summary

This study provides a comprehensive analysis of how ENSO influences precipitation variability in the arid Middle East during the extended cool season (October-May), when the region receives most of its annual rainfall. Understanding how tropical Indo-Pacific SST variability modulates rainfall over the water-scarce Middle East is highly relevant to society, given the profound impacts of drought and flooding on the population, economy, and agriculture. While several of the findings presented in this study have been documented in previous studies, we present here, for the first time, an integrated perspective on the precipitation response to ENSO forcing and the underlying atmospheric drivers. We extend previous work by quantifying the influence of ENSO on precipitation variability at local and regional scales during the cool season and individual months. Furthermore, we employ various diagnostics to quantify the influence of ENSO on the latitudinal position of the subtropical jet stream and the occurrence of Rossby wave breaking and on thermodynamic characteristics such as tropospheric moisture content, moisture transport, and instability. This section summarizes how ENSO forcing shapes the Middle Eastern hydroclimate by synthesizing knowledge from existing studies, complemented with the new findings presented in this study.

Consistent with existing literature (e.g., Price et al., 1998; Nazemosadat and Cordery, 2000; Nazemosadat and Ghasemi, 2004; Mariotti, 2007; Athar, 2015; Kumar et al., 2016; Alizadeh and Mousavizadeh, 2025), we find that El Niño is generally associated with increased precipitation over the Middle East and La Niña with decreased precipitation. The precipitation response to ENSO is asymmetric and varies within the cool season. Anomalies in local and spatially aggregated precipitation are larger during La Niña than during El Niño. Likewise, the slope in spatially aggregated precipitation as a function of the Niño3.4 index is nearly three times larger during La Niña than during El Niño. At intraseasonal scales, precipitation is strongly increased during autumn and moderately enhanced in spring under El Niño conditions. Conversely, during La Niña conditions, precipitation decreases throughout the cool season with significant reductions relative to climatology in autumn and spring. In the core winter months of January and February, precipitation increases under neutral ENSO conditions. The influence of ENSO on Middle East precipitation variability is directly relevant to hydrometeorological hazards. Consecutive La Niña events have been linked to multi-year droughts during the periods of 1999-2001 and 2007-2011 (Barlow et al., 2002; Hoell et al., 2014a). Similarly, El Niño conditions coincided with several devastating floods in the Levant in autumn of 1987, 1994, and 1997 and in the United Arab Emirates in spring 2024 (Krichak et al., 2012; De Vries et al., 2013; Kadhum et al., 2022; Francis et al., 2025; Hussein et al., 2025), corresponding to regions and seasons with increased precipitation under El Niño conditions (Fig. A1).

These precipitation anomalies during the ENSO warm and cold phases are associated with consistent changes in regional circulation patterns over the Middle East. During El Niño conditions, the subtropical jet shifts equatorward, as pointed out by Kumar et al. (2016), Alizadeh-Choobari et al. (2018), and Sandeep and Ajayamohan (2018), accompanied by increased Rossby wave breaking frequencies at the poleward flank and beneath the jet. Consistent with this pattern, a mid-tropospheric cyclonic circulation anomaly dominates over the Middle East along with elevated atmospheric moisture content and strengthened atmospheric moisture transport at its southeastern flank. Likewise, tropospheric conditions are more prone to deep moist convection, facilitated by anomalous warm and moist air advection in the lower troposphere and anomalous cold air in the upper troposphere. Under La Niña conditions, these patterns are reversed. The subtropical jet shifts poleward (cf. Hoell et al., 2024) with a reduction in Rossby wave breaking frequencies at its poleward flank. A mid-tropospheric anticyclonic circulation anomaly emerges, associated with reduced atmospheric moisture content and conditional instability over the Middle East along with weakened atmospheric moisture transport into the region.

These regional precipitation and atmospheric circulation patterns over the Middle East are the combined result of three atmospheric mechanisms (Fig. 13). From a zonal mean perspective, El Niño conditions are associated with an equatorward shift and strengthening of the subtropical jet (Seager et al., 2003, 2005) accompanied by increased Rossby wave breaking at its poleward fringe across North Africa, the Middle East, and southwest-central Asia (Fig. 13a). Anomalous heating in the central Pacific sets up a well-known stationary barotropic Rossby wave pattern arching across North America, the North Atlantic, Europe and North Africa, and culminating in a cyclonic circulation anomaly over the Middle East (Hoell et al., 2013b, 2015a; Kumar et al., 2016). This cyclonic circulation anomaly is merging with a strong upper-tropospheric cyclonic anomaly centered over southeast Asia, which can be understood as a Gill-Matsuno-type response to reduced tropical convection over the tropical Warm Pool, extending westward over South Asia (Barlow et al., 2002; Hoell et al., 2012, 2015a). Consistent with this baroclinic circulation response, an anticyclonic circulation anomaly in the lower troposphere feeds increased warm, moist air masses into transient storms passing by from the west (Mariotti et al., 2005; Mariotti, 2007). La Niña conditions generate opposite circulation patterns, thereby reducing precipitation over the Middle East (Fig. 13b). Besides these three atmospheric pathways, ENSO likely also influences precipitation in the Middle East via its effect on Indian Ocean SSTs and atmospheric conditions (Abid et al., 2020; Hochman and Gildor, 2024). Hence, the distinct seasonal cycle of the Indian Ocean Dipole, mainly active during boreal summer and autumn, may explain why the influence of ENSO on Middle East precipitation varies within the cool season. While our analysis brings together various mechanisms through which tropical Pacific SST forcing modulates precipitation variability over the Middle East, future research may further quantify and disentangle the relative importance of these mechanisms, for example, based on numerical model experiments. Based on our findings, we anticipate that the relative importance of these mechanisms may vary across ENSO phases and seasons.

The findings in this study are subject to several limitations. First, the precipitation dataset used inherits the limitations of the underlying data sources, although qualitatively similar results based on ERA5 precipitation strengthen the confidence in our findings (not shown). Second, our study covers a 42-year period, which inherently limits the sample size of ENSO events and ENSO-like conditions. Third, our analysis does not account for ENSO diversity, such as variations in west-central Pacific SST gradients or the eastward extent of Pacific SST anomalies into the eastern Indian Ocean (Hoell et al., 2013a, 2014b, 2017, 2018), which may modify the Middle Eastern precipitation response. Fourth, our study does not account for non-stationarity in the ENSO-Middle East precipitation relationship, which has been shown to vary across the 20th century (Price et al., 1998; Kang et al., 2015; Hoell et al., 2017; Dasari et al., 2021). Nonetheless, our study provides clear evidence of how ENSO modulates precipitation variability over the Middle East and the underlying atmospheric mechanisms bringing about these precipitation anomalies. Improved process understanding of how tropical Pacific SST variability shapes hydroclimatic conditions in the Middle East is directly relevant to seasonal prediction of precipitation over this water-scarce region, with implications for drought and flood preparedness, as well as for identifying climate model biases and reducing uncertainty in climate projections (Barlow et al., 2021).

Figures

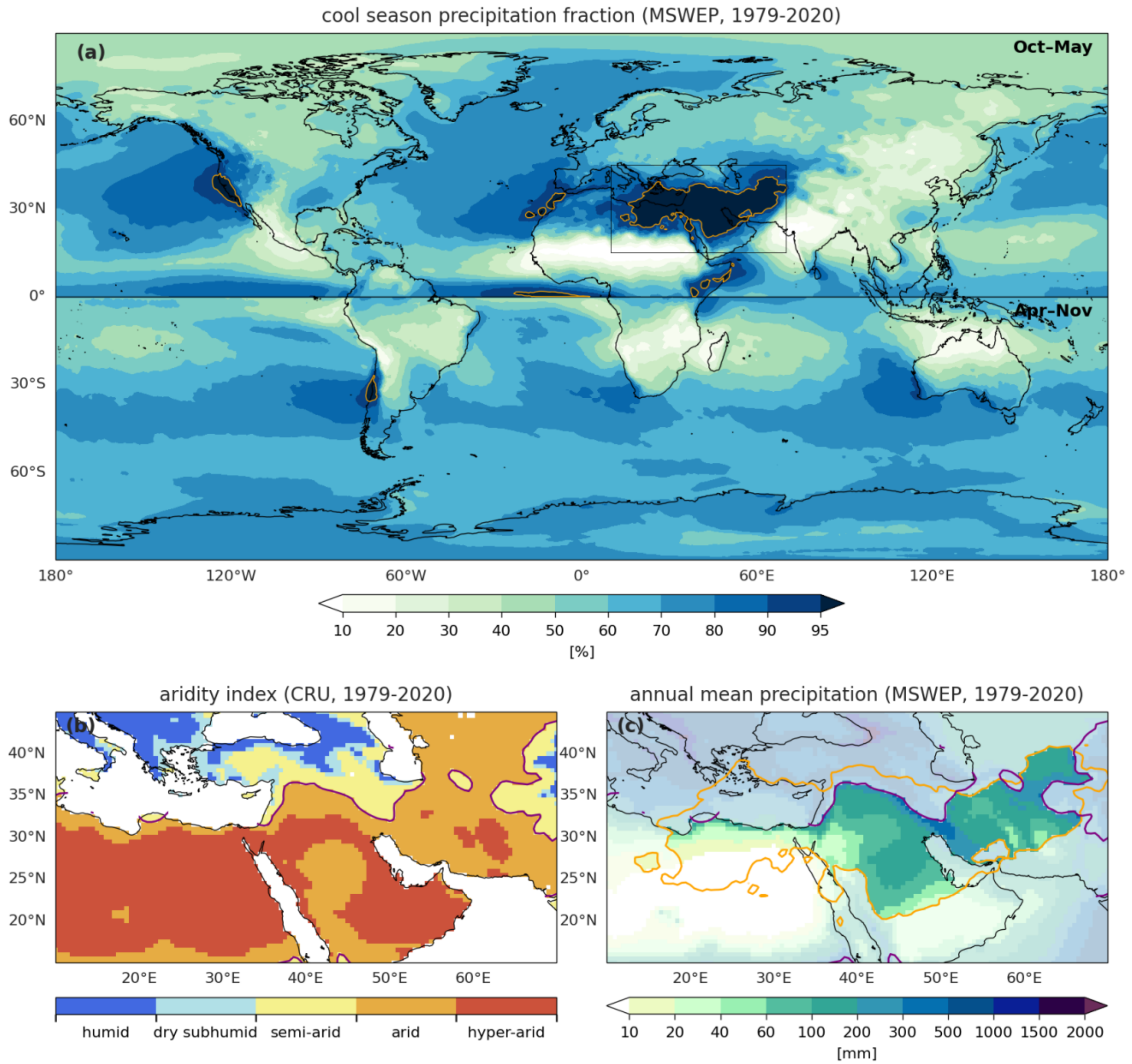

Figure 1. (a) Fractions of cool season precipitation from annual totals in MSWEP (1979-2020) whereby the cool season is defined from October to May in the Northern Hemisphere and from April to November in the Southern Hemisphere; (b) the aridity index across the Middle East region, computed from monthly CRU data (1979-2020) and defined as the ratio of precipitation to potential evapotranspiration; and (c) annual precipitation amounts in MSWEP (1979-2020) in shading, the 95% contour of the cool-season precipitation fraction from the annual total in orange, and the aridity index contour of 0.2, marking an arid to hyper-arid climate, in purple. Opaque shading highlights the target region used for computing spatially aggregated quantities in this study, while areas outside the target region are plotted in semi-transparent colors.

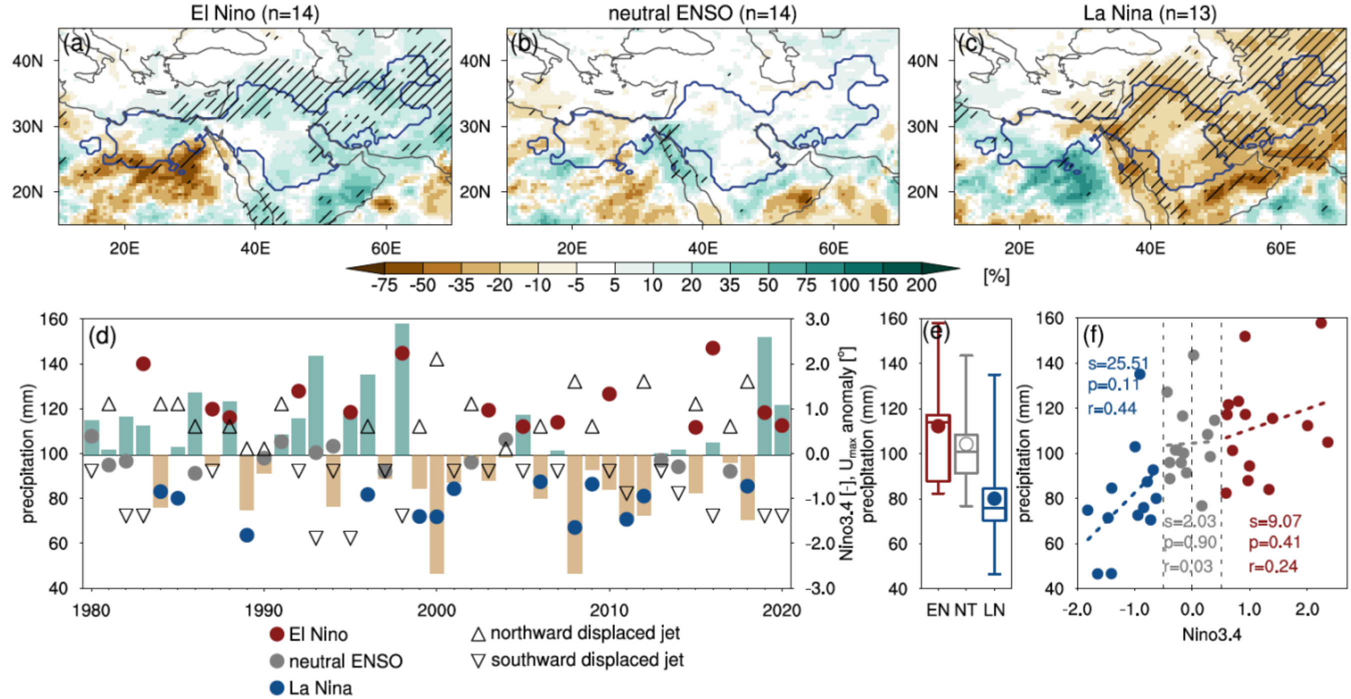

Figure 2. The spatial, temporal, and statistical distribution of cool-season precipitation in the Middle East and ENSO represented by the Nino3.4 index. Relative precipitation anomalies during the cool season for (a) El Niño, (b) neutral ENSO, and (c) La Niña events from climatology. The numbers in the figure title denote the number of ENSO events and the blue contour highlights the region of interest; see the text for details. Hatching denotes statistical significance based on a Monte Carlo test with 10,000 randomly drawn samples and applying a two-sided test at the $p < 0.05$ significance level. (d) Timeseries of cool season precipitation (not detrended) amounts in the bars in green and brown colors for values larger and smaller than the multi-year annual mean, and the Nino3.4 index based on the 5-monthly running mean SST anomalies from October to February in red, grey, and blue dots representing the ENSO warm, neutral, and cold phases, respectively. Upward and downward pointing triangles indicate the poleward and equatorward displacements of the subtropical jet over the Middle East region, respectively. The years on the x-axis refer to Oct-Dec of the previous year and Jan-May of the current year; for example, 1980 represents Oct-Dec 1979 and Jan-May 1980. (e) The distribution of spatially aggregated precipitation with the boxes showing the interquartile range, the whiskers the minimum and maximum values, the line in the middle the median, and the circles the mean, filled at the $p < 0.05$ significance level and open circles for non-significant values relative to climatology. (f) The relationship of precipitation with the Nino3.4 index with the text indicating the slope (s) of precipitation based on linear regression, the p-value (p) of this regression coefficient, and the correlation (r) for Nino3.4 values corresponding to the El Nino, neutral ENSO, and La Nina phases in red, gray, and blue text, respectively.

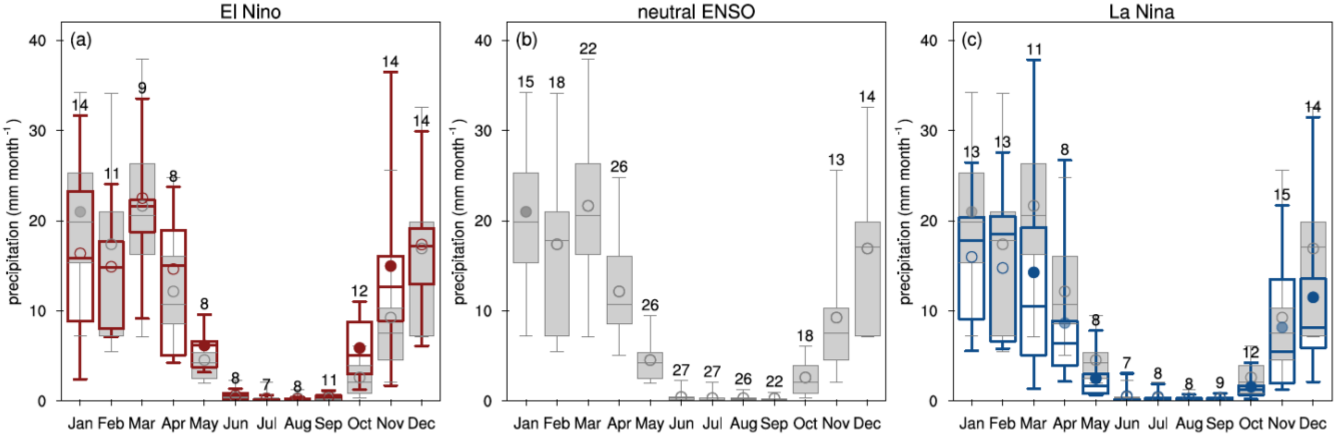

Figure 3. Monthly distribution of spatially aggregated non-detrended precipitation for (a) El Niño, (b) neutral ENSO, and (c) La Niña conditions based on the Nino3.4 index computed from 3-monthly running mean SST anomalies. The boxes denote the lower and upper quartiles, the whiskers the minimum and maximum values, and the line in the middle the median. The spatially aggregated mean is shown by the circles, filled at the $p < 0.05$ significance level, semi-transparent at the $p < 0.1$ level, and open circles for non-significance anomalies relative to climatology. The sample sizes are indicated in the number above the boxes. The distribution of neutral ENSO conditions is overlaid in grey for reference for the El Niño and La Niña phases in (a) and (c).

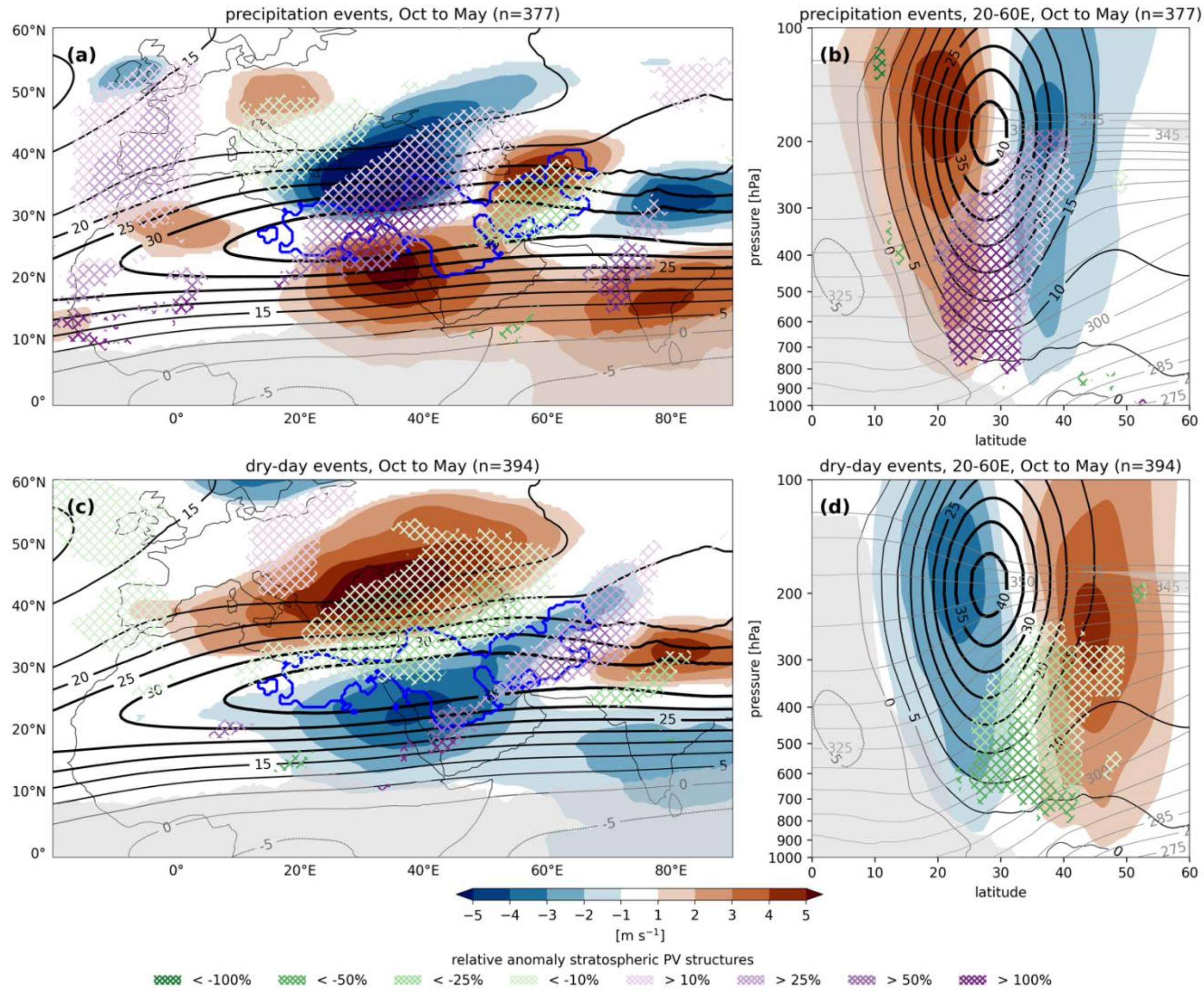

Figure 4. Composites of anomalies in zonal wind and Rossby wave breaking frequencies based on the onset of (a, b) precipitation events and (c,d) dry-day events. (a,c) 250-hPa zonal wind anomalies in colors and relative anomalies of stratospheric PV structure frequencies – aggregated over 300-350K - in hatching, as indicated by the legend. (b,d) The zonal mean (20-60E) zonal wind anomalies in colors and relative anomalies of stratospheric PV structure frequencies in hatching at pressure levels interpolated from data on isentropic surfaces between 275 and 360 K with 5 K intervals. These isentropic surfaces are plotted in grey contours. Zonal wind and Rossby wave breaking anomalies are shown only where considered significant at $p < 0.05$ based on a Monte Carlo test with 1,000 samples. Gray shading marks regions where climatological frequencies of vertically aggregated PV structure occurrences over 300-350K in (a,c) are below 25 counts and of PV structure occurrences in (b,d) fall below 5 counts. The region of interest is denoted in blue contours in (a,c) for reference. Sample sizes of precipitation and dry-day events are indicated in the figure titles.

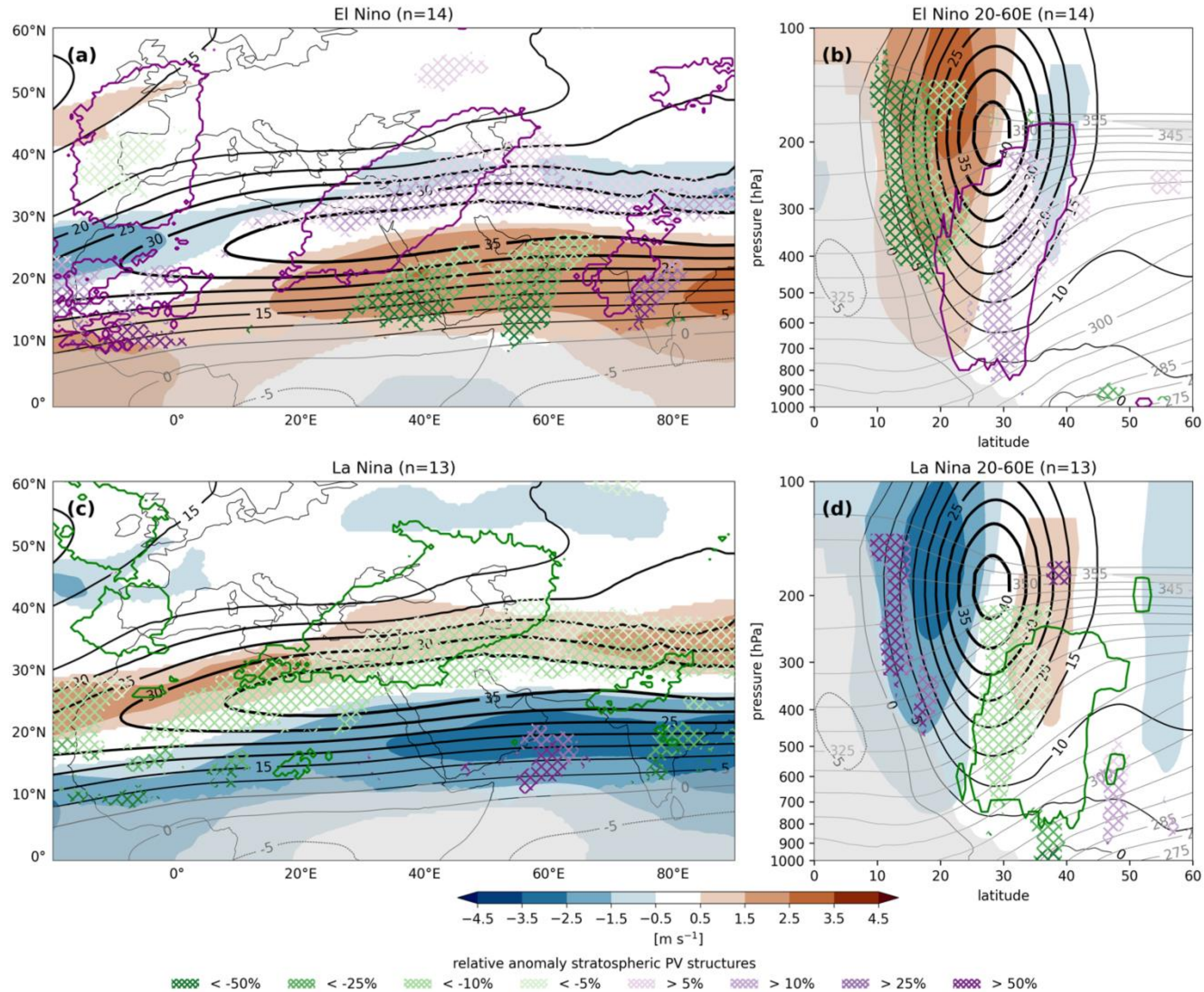

Figure 5. Composites of anomalies in cool-season zonal wind and Rossby wave breaking frequencies for (a,b) El Niño and (c,d) La Niña events. (a,c) 250-hPa zonal wind anomalies in colors and relative anomalies of stratospheric PV structure frequencies – aggregated over 300-350K - in hatching, as indicated by the legend. (b,d) The zonal mean (20-60°E) zonal wind anomalies in colors and relative anomalies of stratospheric PV structure frequencies in hatching at pressure levels interpolated from data on isentropic surfaces between 275 and 360 K with 5 K intervals. These isentropic surfaces are plotted in grey contours. Zonal wind and Rossby wave breaking anomalies are only shown where considered significant at $p < 0.1$. Gray shading denotes regions where climatological frequencies of vertically aggregated PV structure occurrences over 300-350K in (a,c) are below 25 counts and of PV structure occurrences in (b,d) fall below 5 counts. For reference, regions where relative anomalies in stratospheric PV structure frequencies exceed 10% for precipitation events are outlined in green contours in (a,b), while those falling below -10% for dry-day events are outlined in purple contours in (c,d).

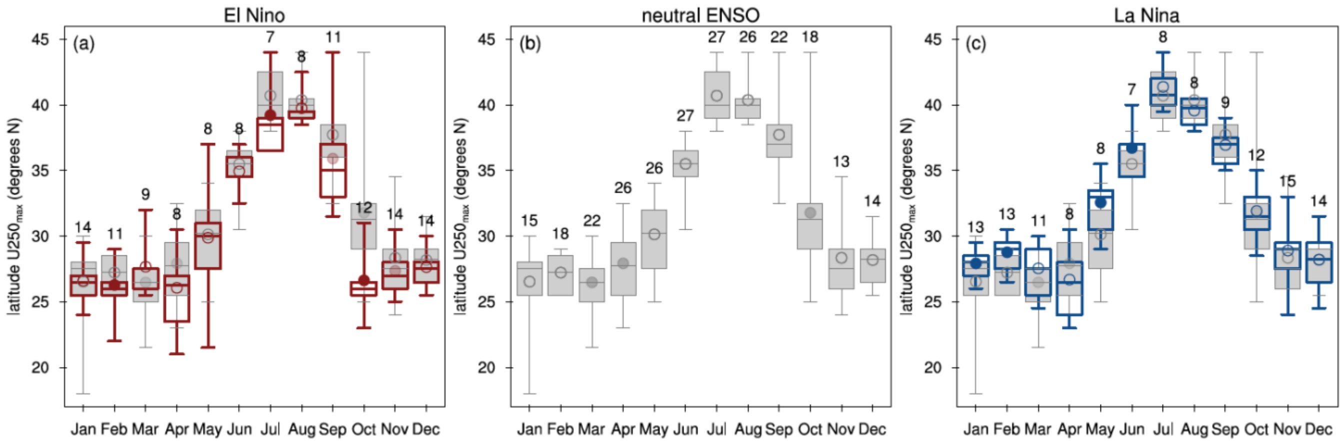

Figure 6. Monthly distribution of the latitudinal position of the subtropical jet axis for (a) El Niño, (b) neutral ENSO, and (c) La Niña conditions. The latitudinal position of the subtropical jet is defined by the maxima in the zonal mean (20-60°E) of the non-detrended monthly mean 250-hPa zonal wind between 18-44°N. The boxes denote the lower and upper quartiles, the whiskers the minimum and maximum values, and the line in the middle the median. The mean jet position is depicted by circles, filled at the $p < 0.05$ significance level, semi-transparent at the $p < 0.1$ level, and open circles for non-significance anomalies relative to climatology. The sample sizes are indicated by the numbers above the boxes. The distribution of neutral ENSO conditions is overlaid in grey for reference for the El Nino and La Nina conditions in (a) and (c).

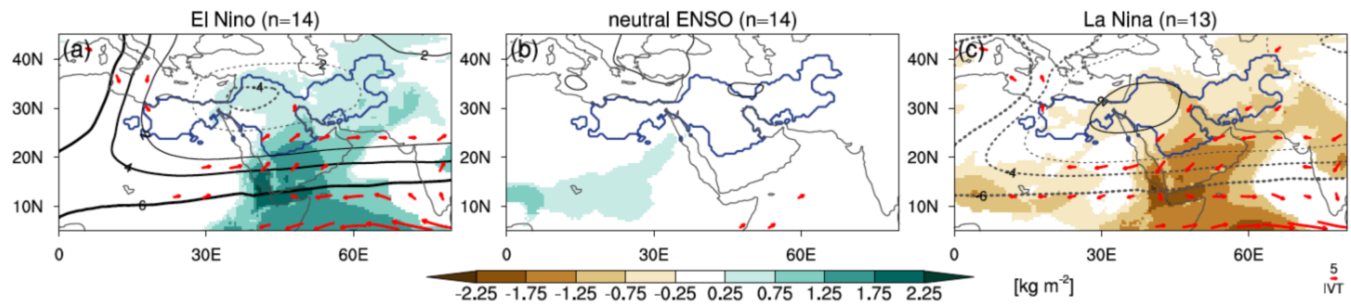

Figure 7. Composites of cool-season anomalies in total column water (kg m^{-2}) in colors, vertically integrated horizontal water vapor transport (kg m^{-1} s^{-1}) in red vectors, and 500-hPa geopotential height (m) in solid and dashed black contours for positive and negative values, respectively, for (a) El-Niño, (b) neutral ENSO, and (c) La Niña events. Anomalies in total column water are only plotted where significant at the $p < 0.05$ level. The numbers in the figure title denote the number of samples for each ENSO phase, and the blue contour highlights the region of interest.

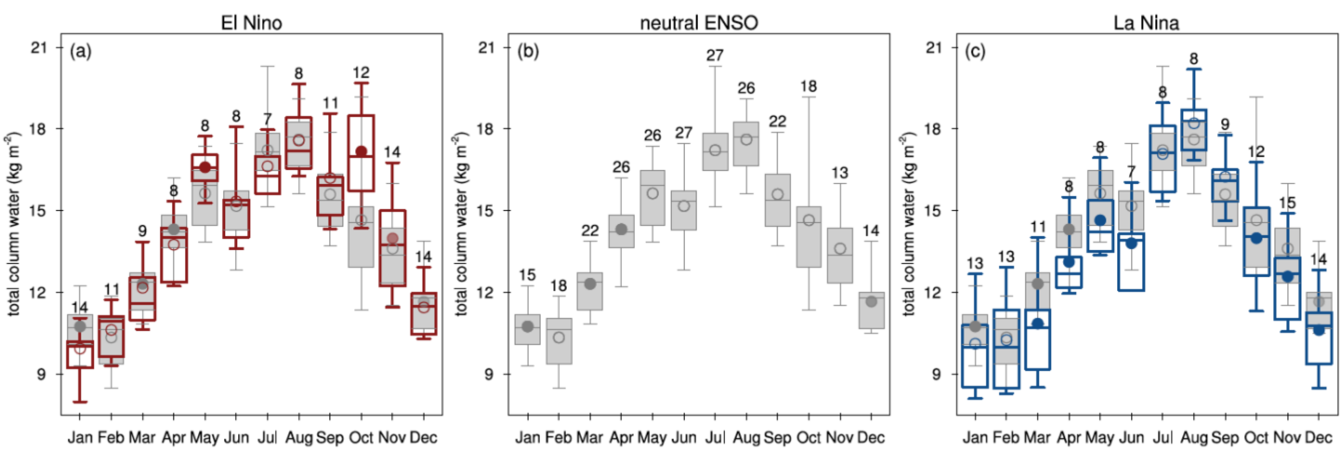

Figure 8. Monthly distribution of spatially aggregated non-detrended total column water for (a) El Niño, (b) neutral ENSO, and (c) La Niña conditions. The boxes denote the lower and upper quartiles, the whiskers the minimum and maximum values, the line in the middle the median, and the circle the mean, filled at the $p < 0.05$ significance level, semi-transparent at the $p < 0.1$ level, and open circles for non-significance anomalies relative to climatology. The sample sizes are indicated by the numbers above the boxes. The distribution of neutral ENSO conditions is overlaid in grey for reference for the El Niño and La Niña phases in (a) and (c).

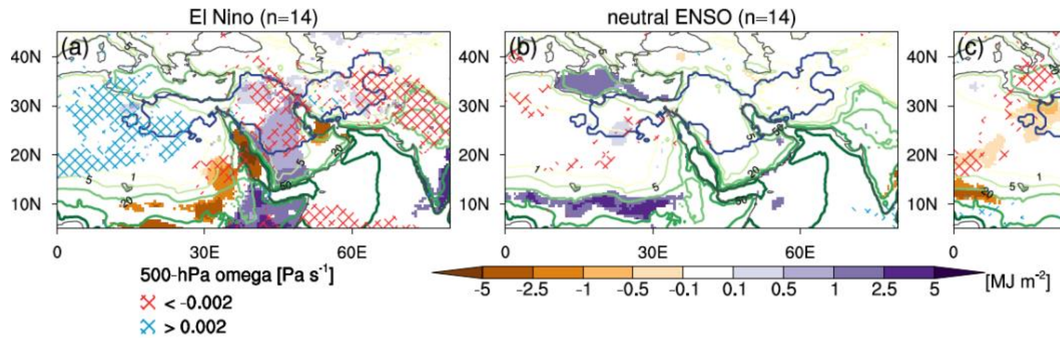

Figure 9. Composites of cool-season anomalies in I_{max} [MJ m^{-2}] in colors for (a) El-Niño, (b) neutral ENSO, and (c) La Niña events. Yellow-green contours show the climatological distribution of I_{max} at intervals of 1, 5, 20, 50, and 100 MJ m^{-2}. Red and blue hatching mark regions with anomalous 500-hPa omega falling below -0.002 Pa s-1 (ascent) and exceeding 0.002 Pa s-1 (descent). Anomalies in I_{max} and 500-hPa omega are only plotted where significant at the $p < 0.05$ level. The numbers in the figure title indicate the number of samples for each ENSO phase, and the blue contour highlights the region of interest.

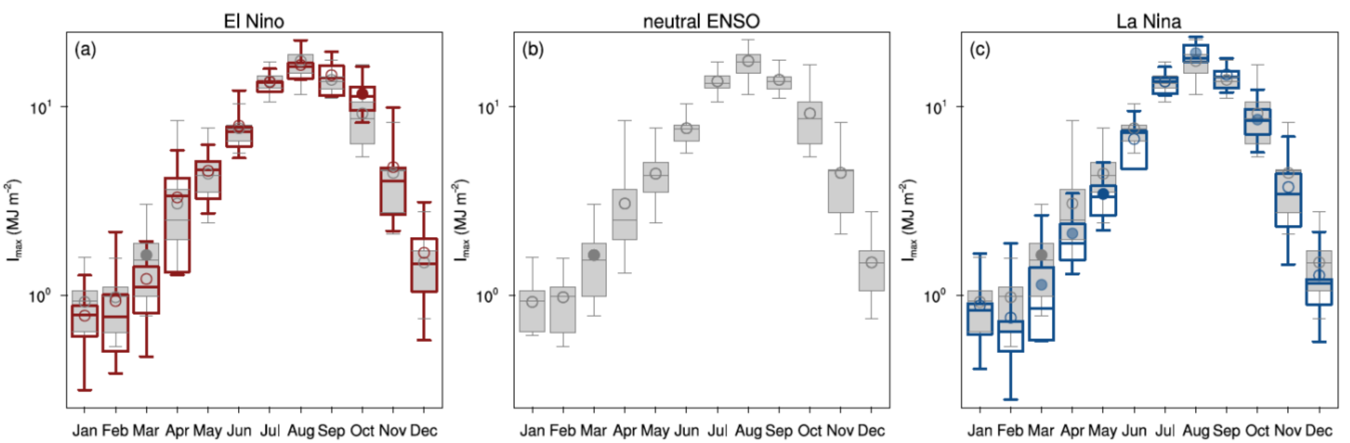

Figure 10. Monthly distribution of spatially aggregated non-detrended I_{max} for (a) El-Niño, (b) neutral ENSO, and (c) La Niña conditions. The boxes denote the lower and upper quartiles, the whiskers the minimum and maximum values, the line in the middle the median, and the circle the mean, filled at the $p < 0.05$ significance level, semi-transparent at the $p < 0.1$ level, and open circles for non-significance anomalies relative to climatology. The distribution of neutral ENSO conditions is overlaid in grey for reference for the El Nino and La Nina phases in (a) and (c).

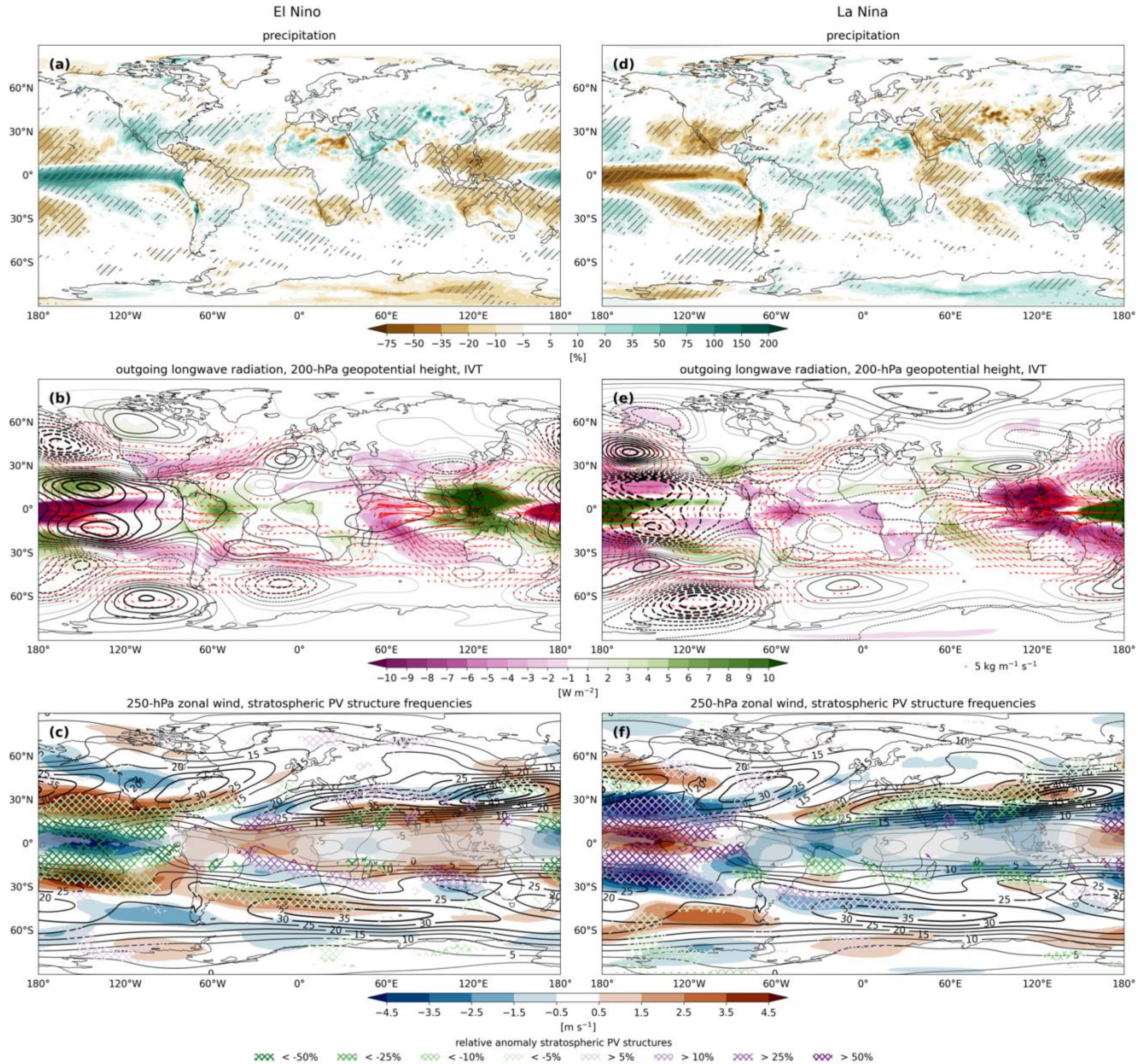

Figure 11. Composites of cool-season anomalies for (a-c) El-Niño and (d-f) La Niña. In (a,d) relative precipitation anomalies (%) from MSWEP, (b,e) top thermal radiation (W m^{-2}) in colors with negative anomalies corresponding to enhanced tropical convection and positive anomalies to reduced convection, 200-hPa geopotential height (m) contours at 4 gpm intervals with positive and negative values in solid and dashed lines, respectively, and vertically integrated horizontal water vapor transport (kg m^{-1} s^{-1}) in red vectors, and (c,f) 250-hPa zonal wind anomalies (m s^{-1}) in colors, the climatological mean of 250-hPa zonal wind in contours at 5 m s^{-1} intervals, and relative anomalies in stratospheric PV structure occurrences, aggregated over 300-350K, in hatching, as indicated by the legend. Anomalies in top thermal radiation are only shown where considered significant at $p < 0.05$ and in zonal wind and Rossby wave breaking frequencies where considered significant at $p < 0.1$.

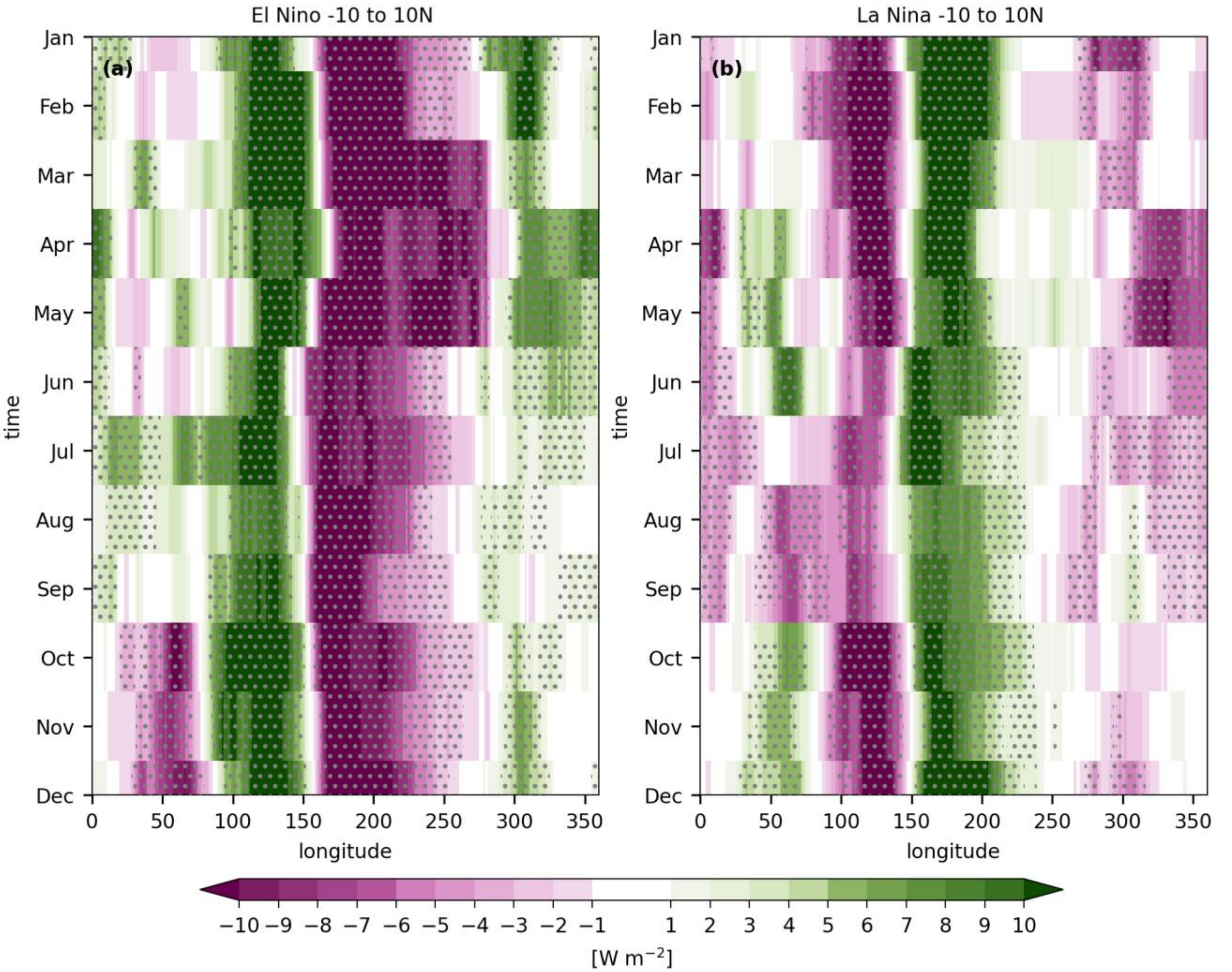

Figure 12. Hovmöller diagrams with anomalies in the Equatorial average (10°S-10°N) outgoing longwave radiation as a function of longitude and time for (a) El Niño and (b) La Niña conditions with negative anomalies corresponding to enhanced tropical convection and positive anomalies to reduced convection.

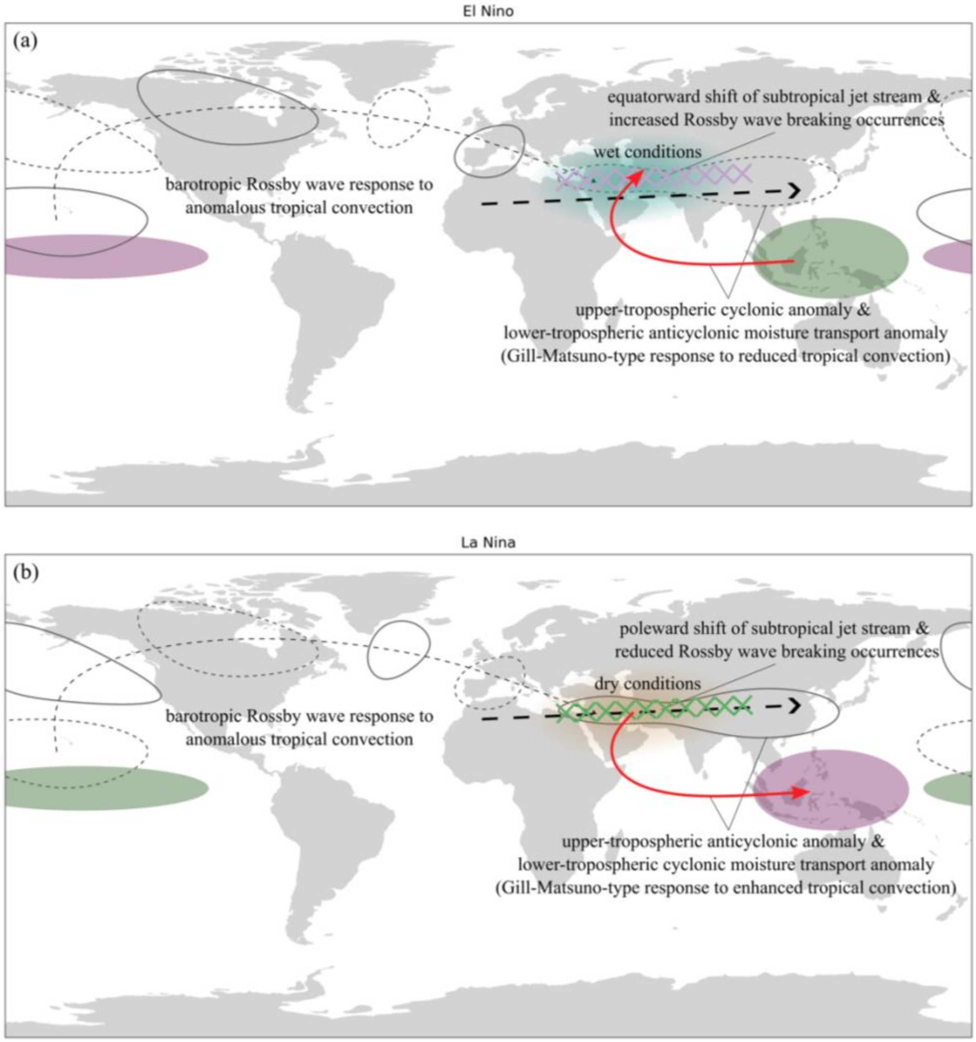

Figure 13. A schematic representation of three different mechanism through which ENSO modulates Middle Eastern precipitation variability during the cool season under (a) El Niño and (b) La Niña conditions: (1) a zonally symmetric displacement of the subtropical jet (cf. Kumar et al., 2016; Alizadeh-Choobari et al., 2018; Sandeep and Ajayamohan, 2018; Hoell et al., 2024) alongside modifications in Rossby wave breaking occurrences on the poleward flank and beneath the jet core, (2) a barotropic Rossby wave response arching from the tropical Pacific via the extratropics toward the Middle East (cf. Kumar et al., 2016; Hoell et al., 2013b; Hoell et al., 2015a; Abid et al., 2020), and (3) a regional baroclinic response in the tropical circulation extending westwards from the tropical Warm Pool, consistent with a Gill-Matsuno- type response (cf. Barlow et al., 2002; Hoell et al., 2012; Hoell et al., 2015a). This schematic is inspired by Fig. 9 from Barlow et al. (2016), showing mechanism (2) and (3) for La Niña conditions.

Appendix A

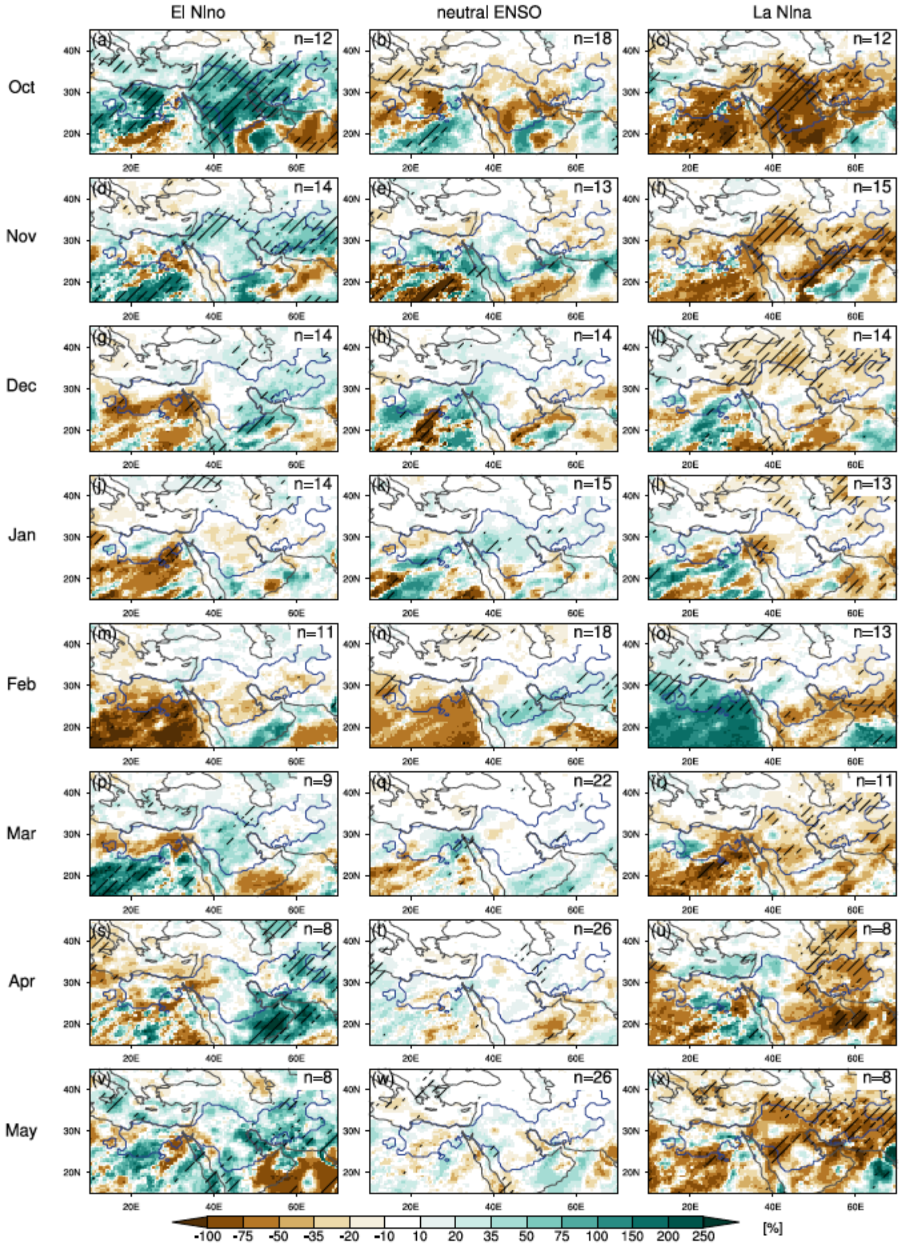

685 **Figure A1. As Fig. 2a,b,c but for individual months from October to May. The ENSO phases are defined based on 3-monthly running mean SST anomalies in the Nino3.4 region. Sample sizes are indicated in text in the top right corner of each panel.**

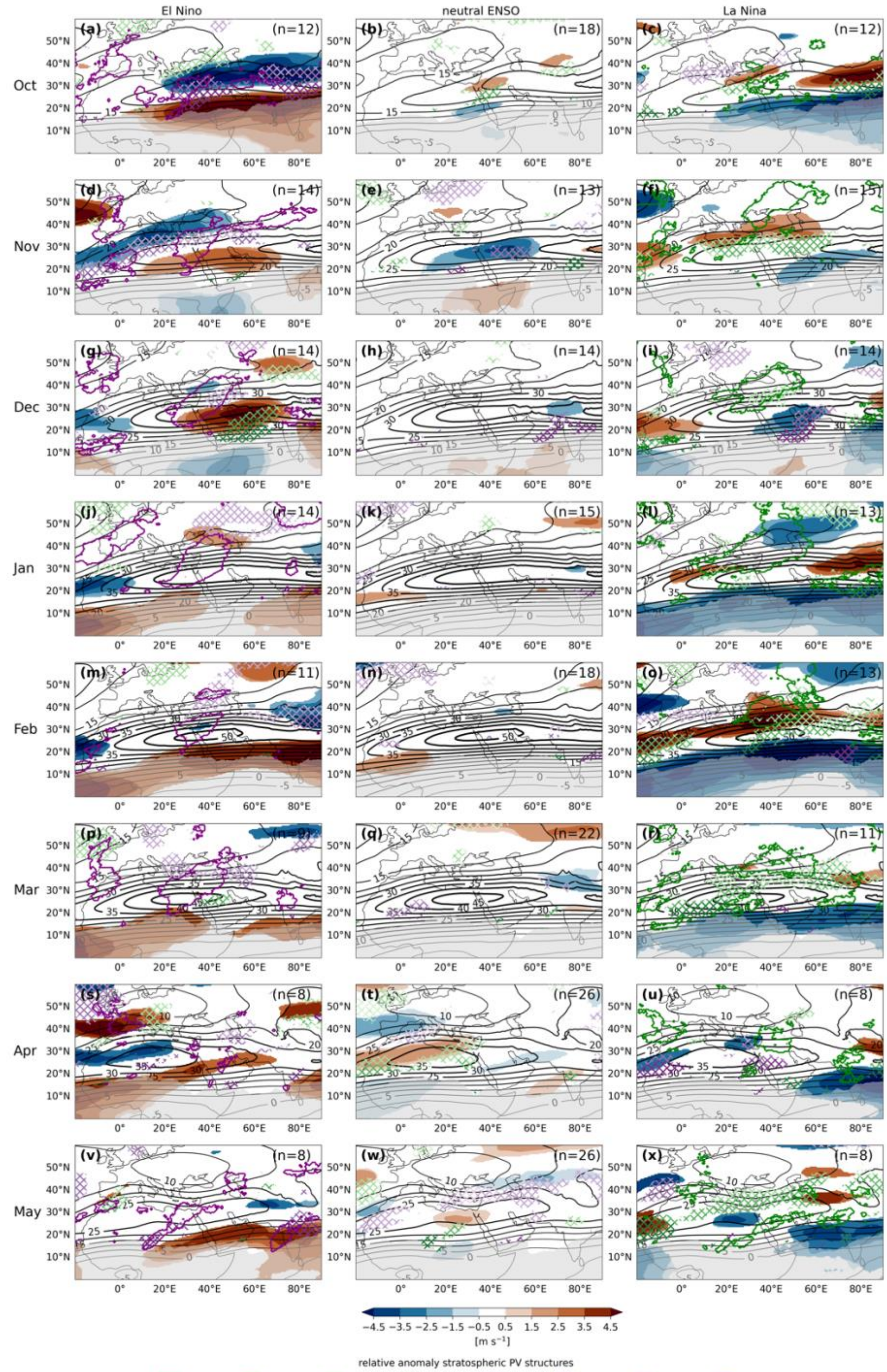

Figure A2. As Fig. 5(a,c) but for individual months from October to May in rows and the ENSO phases - warm, neutral, and cold - in columns. The ENSO phases are defined based on 3-monthly running mean SST anomalies in the Nino3.4 region. Sample sizes are indicated in text in the top right corner of each panel.

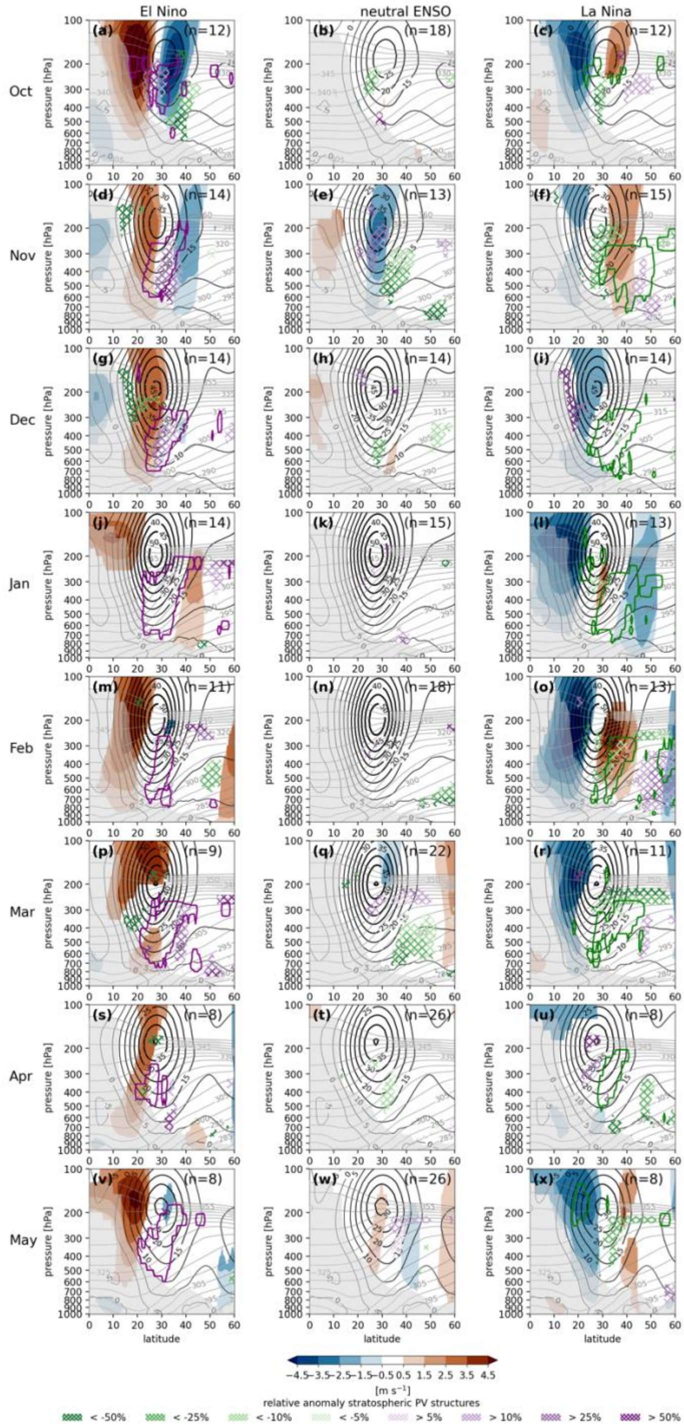

Figure A3. As Fig. 5(b,d) but for individual months from October to May in rows and the ENSO phases - warm, neutral, and cold - in columns. The ENSO phases are defined based on 3-monthly running mean SST anomalies in the Nino3.4 region. Sample sizes are indicated in text in the top right corner of each panel.

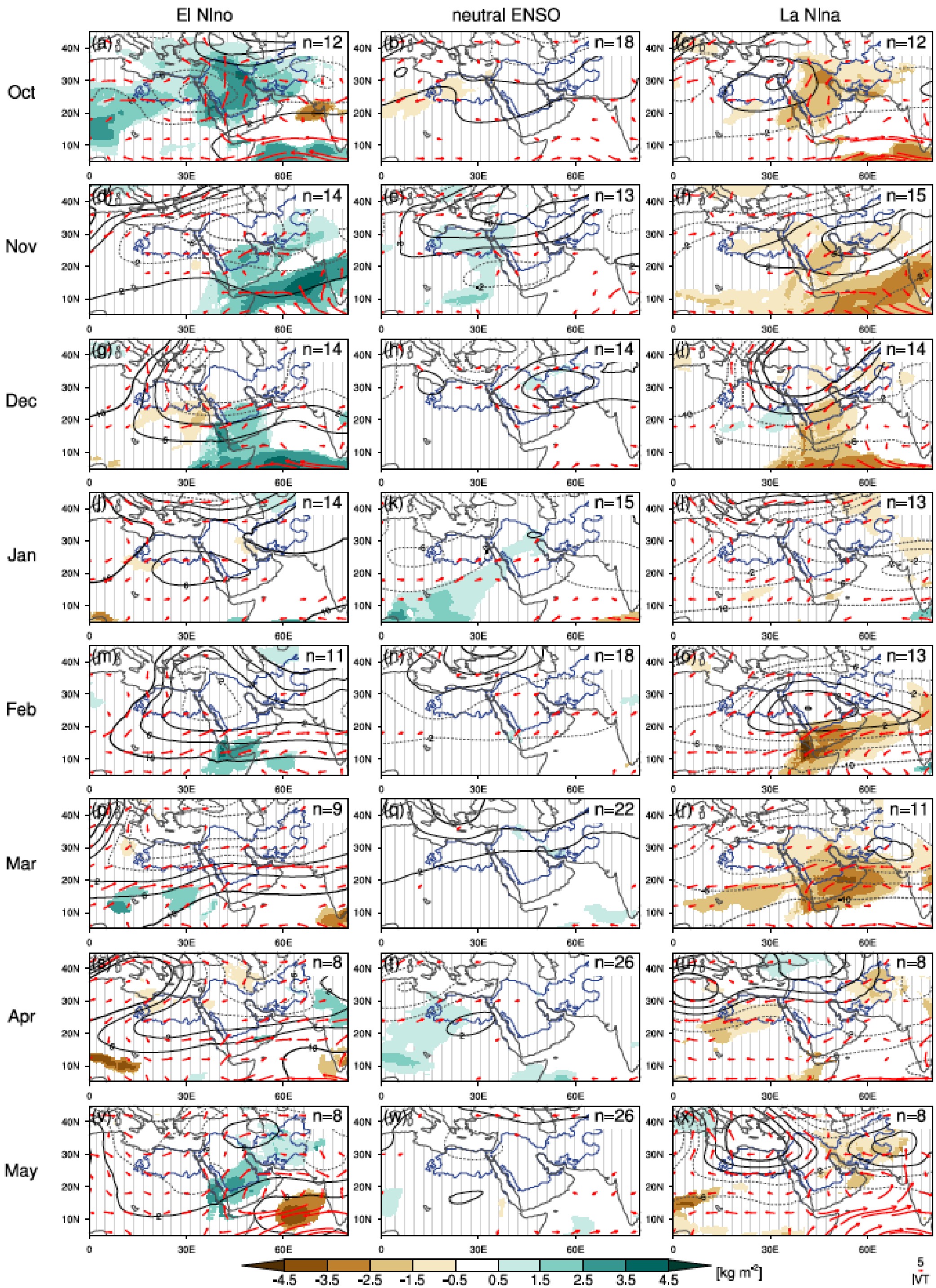

695

Figure A4. As Fig. 7 but for individual months from October to May in rows and the ENSO phases - warm, neutral, and cold - in columns. The ENSO phases are defined based on 3-monthly running mean SST anomalies in the Nino3.4 region. Sample sizes are indicated in text in the top right corner of each panel.

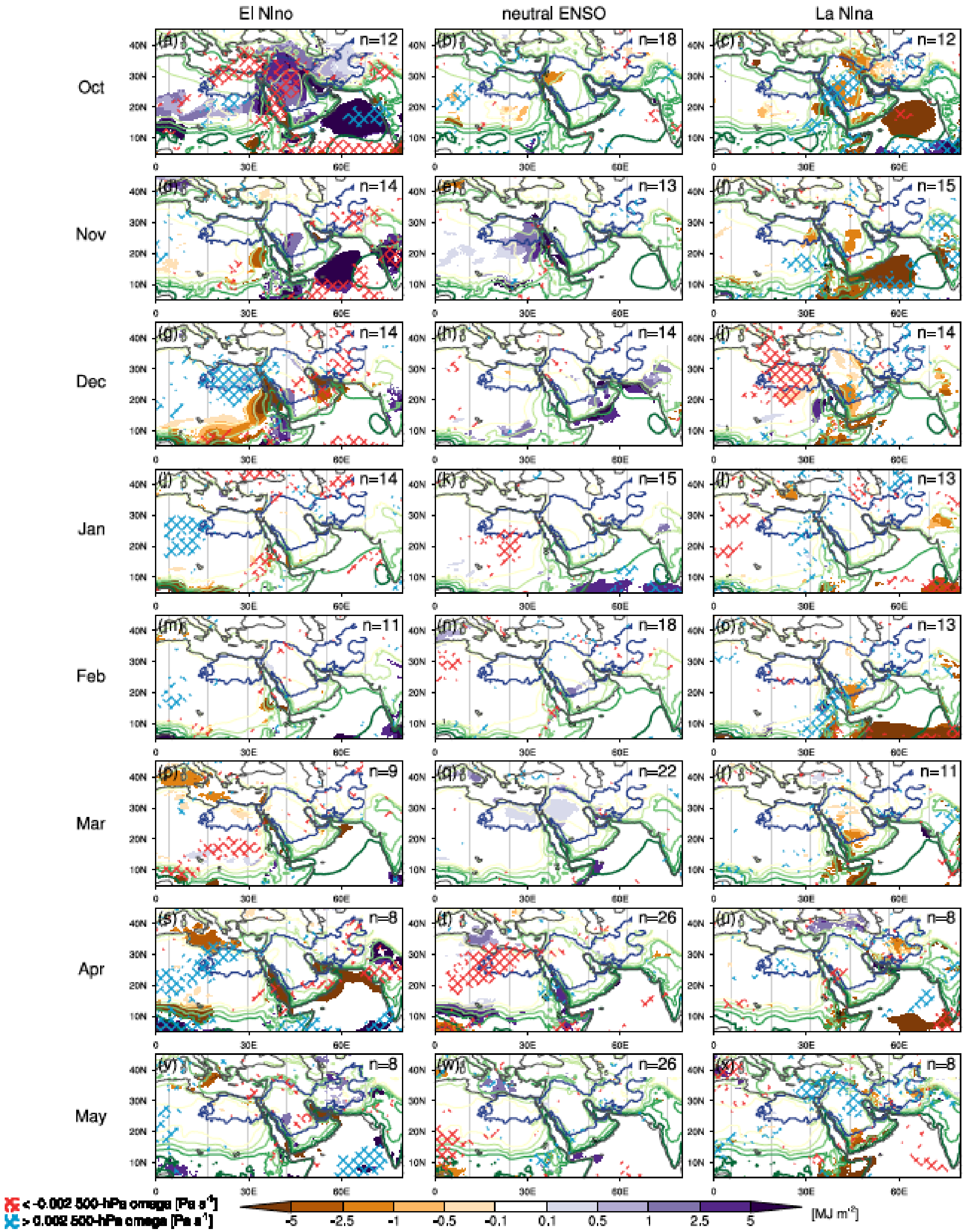

700 **Figure A5. As Fig. 9 but for individual months from October to May in rows and the ENSO phases - warm, neutral, and cold - in columns. The ENSO phases are defined based on 3-monthly running mean SST anomalies in the Nino3.4 region. Sample sizes are indicated in text in the top right corner of each panel.**

Code and data availability

All datasets used in this study are freely available from respective data providers. ERA5 data from the ECMWF was downloaded from the MARS archive and is also available from the Climate Data Store (https://cds.climate.copernicus.eu/). MSWEP from GloH2O was retrieved from the web (https://www.gloh2o.org). ERSSTv6 from NOAA is publicly available (https://www.ncei.noaa.gov/products/extended-reconstructed-sst).

Author contributions

AJV developed the idea for this study. AJV, JWC, GF provided data used in this study. AJV analyzed and visualized the data used in this study and SFB contributed to the analysis and interpretation of the results. AJV wrote the initial draft of this manuscript. All authors contributed to reviewing and editing of the manuscript.

Competing interests

At least one of the (co-)authors is a member of the editorial board of Weather and Climate Dynamics.

Acknowledgements

The authors thank N. C. G Hart for helpful discussions on the metric to diagnose tropospheric instability. We also thank Mathew Barlow and Dor Sandler for providing constructive and thoughtful reviews that helped us improving the manuscript.

Financial support

JWC acknowledges the US National Science Foundation award #2202663. D.D. acknowledges support from the Swiss National Science Foundation through project PP00P2_198896.

References

Abid, M. A., Kucharski, F., Almazroui, M., and Kang, I.-S.: Interannual rainfall variability and ECMWF-Sys4-based predictability over the Arabian Peninsula winter monsoon region, Q. J. Roy. Meteor. Soc., 142, 694, 233-242, https://doi.org/10.1002/qj.2648, 2016.

Abid, M. A., Ashfaq, M., Kucharski, F., Evans, K., and Almazroui, M.: Tropical Indian Ocean mediates ENSO influence over central southwest Asia during the wet season, Geophys. Res. Lett, 47, 18, e2020GL089308, https://doi.org/10.1029/2020GL089308, 2020.

Alizadeh-Choobari, O., Adibi, P., and Irannejad, P.: Impact of the El Niño-Southern Oscillation on the climate of Iran using ERA-Interim data, Clim. Dyn., 51,2897-2911, https://link.springer.com/article/10.1007/s00382-017-4055-5, 2018.

Alizadeh, O., and Mousavizadeh, M.: Impact of ENSO on extreme precipitation in Southwest Asia, Glob. Plan. Change, 244, 104645, https://doi.org/10.1016/j.gloplacha.2024.104645, 2025.

Armon, M., Shmilovitz, Y., and Dente, E.: Anatomy of a Foreseeable Disaster: Lessons from the 2023 Dam-Breaching Flood in Derna, Libya, Science Advances, 11, 13, https://doi.org/10.1126/sciadv.adu2865, 2025.

Athar, H.: Teleconnections and variability in observed rainfall over Saudi Arabia during 1978-2010, Atmos. Sci., Lett., 16, 373-379, https://doi.org/10.1002/asl2.570, 2015.

Bahrami, F., Saadatabadi, A. R., Meshkatee, A. H., Kamali, G.: The impact of ENSO phase transition on the atmospheric circulation, precipitation, and temperature in the Middle East autumn, Asia-Pacific J. Atmos. Sci, 56, 439-453, https://link.springer.com/article/10.1007/s13143-019-00149-2, 2021.

Barlow, M., Cullen, H., and Lyon, B.: Drought in central and southwest Asia: La Niña, the warm pool, and Indian Ocean precipitation, J. Climate, 15, 697–700, https://doi.org/10.1175/1520-0442(2002)015%3C0697:DICASA%3E2.0.CO;2, 2002.

Barlow, M., Wheeler, M., Lyon, B., and Cullen, H.: Modulation of daily precipitation over southwest Asia by the Madden-Julian Oscillation, Mon. Weath, Rev., 3579-3594, https://doi.org/10.1175/MWR3026.1, 2005.

Barlow, M., Hoell, A., and Colby, F.: Examining the wintertime response to tropical convection over the Indian Ocean by modifying convective heating in a full atmospheric model, Geophys. Res. Lett, 34, L19702, https://doi.org/10.1029/2007GL030043, 2007.

Barlow, M., Zaitchik, B., Paz, S., Black, E., Evans, J., and Hoell, A.: A Review of Drought in the Middle East and Southwest Asia, J. Climate, 29, 8547–8574, https://doi.org/10.1175/JCLI-D-13-00692.1, 2016.

Barlow, M., Hoell, A., and Agel, L.: An evaluation of CMIP6 historical simulations of the cold season teleconnection between tropical Indo-Pacific Sea surface temperatures and precipitation in southwest Asia, the coastal Middle East, and northern Pakistan and India, J. Climate, 34,16, 6905-6926, https://doi.org/10.1175/JCLI-D-19-1026.1, 2021.

Beck, H. E., Wood, E. F., Pan, M., Fisher, C. K., Miralles, D. G., van Dijk, A. I., McVicar, T. R., and Adler, R. F.: MSWEP V2 global 3-hourly 0.1 precipitation: methodology and quantitative assessment, B. Am. Meteorol. Soc., 100, 473–500, https://doi.org/10.1175/BAMS-D-17-0138.1, 2019.

Bharati, P., Deb, P., Hunt, K. R., Orr, A., Dash, M. K.: ENSO-induced latitudinal variation of the subtropical jet modulates extreme winter precipitation over the western Himalayas, Adv. Atmos., Sci., 42, 427-437, https://link.springer.com/article/10.1007/s00376-024-4057-2, 2025.

Cannon, F., Carvalho, L. M. V., Jones, C., Hoell, A., Norris, J., Kiladis, G. N., and Tahir, A. A.: The influence of tropical forcing on extreme winter precipitation in the western Himalaya, Clim. Dynam., 48, 1213–1232, https://doi.org/10.1007/s00382-016-3137-0, 2017.

Casselman, J. W., Taschetto, A. S., and Domeisen, D. I.: Nonlinearity in the pathway of El Niño-Southern Oscillation to the tropical North Atlantic, J. Climate, 34, 7277–7296, https://doi.org/10.1175/jcli-d-20-0952.1, 2021.

Chakraborty, A., Behera, S. K., Mujumdar, M., Ohba, R., and Yamagata, T.: Diagnosis of tropospheric moisture over Saudi Arabia and influences of IOD and ENSO, Mon. Weather Rev., 134, 598–617, https://doi.org/10.1175/MWR3085.1, 2006.

Coleman, M., de Vries, A. J., Roberts, C., and Domeisen, D.I.V.: Floods in the European Union and the Middle East and North Africa region: Socio-economic impacts, characteristics, and perception, under review in Nat. Haz. Earth Syst. Env, https://egusphere.copernicus.org/preprints/2026/egusphere-2026-1827/.

Dasari, H. P., Desamsetti, S., Langodan, S., Attada, R., Ashok, K., and Hoteit, I.: Long-term changes in the Arabian Peninsula rainfall and their relationship with the ENSO signals in the tropical Indo-Pacific, Clim. Dyn., 59, 1715-1731, https://link.springer.com/article/10.1007/s00382-021-06062-7, 2021.

de Vries, A. J., Tyrlis, E., Edry, D., Krichak, S. O., Steil, B., and Lelieveld, J.: Extreme precipitation events in the Middle East: Dynamics of the Active Red Sea Trough, J. Geophys. Res.-Atmos., 118, 7087–7108, https://doi.org/10.1002/jgrd.50569, 2013.

de Vries, A. J., Feldstein, S. B., Riemer, M., Tyrlis, E., Sprenger, M., Baumgart, M., Fnais, M., and Lelieveld, J.: Dynamics of tropical-extratropical interactions and extreme precipitation events in Saudi Arabia in autumn, winter and spring, Q. J. Roy. Meteor. Soc., 142, 1862–1880, https://doi.org/10.1002/qj.2781, 2016.

de Vries, A. J., Ouwersloot, H. G., Feldstein, S. B., Riemer, M., El Kenawy, A. M., McCabe, M. F., and Lelieveld, J.: Identification of tropical-extratropical interactions and extreme precipitation events in the Middle East based on potential vorticity and moisture transport, J. Geophys. Res.-Atmos., 123, 861–881, https://doi.org/10.1002/2017JD027587, 2018.

de Vries, A. J., Armon, M., Klingmüller, K., Portmann, R., Röthlisberger, M., Domeisen, D. I. V.: Breaking Rossby waves drive extreme precipitation in the world's arid regions, Commun. Earth & Env., 5, 493, https://www.nature.com/articles/s43247-024-01633-y, 2024.

de Vries, A. J.: A global climatological perspective on the importance of Rossby wave breaking and intense moisture transport for extreme precipitation events, Weather Clim. Dynam., 2, 129–161, https://doi.org/10.5194/wcd-2-129-2021, 2021.

Francis, D., Fonseca, R., Nelli, N., Cherif, C., Yarragunta, Y., Zittis, G., and de Vries, A. J.: From cause to consequence: examining the historic April 2024 rainstorm in the United Arab Emirates through the lens of climate change, npj Clim.Atmos. Sci., 8, 183, https://www.nature.com/articles/s41612-025-01073-1, 2025.

Gill, A. E.: Some simple solutions for heat-induced tropical circulation, Q. J. Roy. Meteor. Soc., 106, 447-462, https://doi.org/10.1002/qj.49710644905, 1980.

Gleick, P. H.: Water, drought, climate change, and conflict in Syria, Weather Clim. Soc. 6, 331–340, https://doi.org/10.1175/WCAS-D-13-00059.1, 2014.

Haris, I., Osborn, T. J., Jones, P. and Lister, D.: Version 4 of the CRU TS monthly high-resolution gridded multivariate climate datasets. Sci. Data, 7, 109, https://www.nature.com/articles/s41597-020-0453-3, 2020.

Hart, N. C. G., Washington, R., and Reason, C. J. C.: On the likelihood of tropical-extratropical cloud bands in the South Indian Convergence one during ENSO events, J. Climate, 31, 7, 2797-2817, https://doi.org/10.1175/JCLI-D-17-0221.1, 2018.

Hersbach, H., Bell, B., Berrisford, P., Hirahara, S., Horányi, A., Muñoz-Sabater, J., Nicolas, J., Peubey, C., Radu, R., Schepers, D., Simmons, A., Soci, C., Abdalla, S., Abellan, X., Balsamo, G., Bechtold, P., Biavati, G., Bidlot, J., Bonavita, M., De Chiara, G., Dahlgren, P., Dee, D., Diamantakis, M., Dragani, R., Flemming, J., Forbes, R., Fuentes, M., Geer, A., Haimberger, L., Healy, S., Hogan, R. J., Hólm, E., Janisková, M., Keeley, S., Laloyaux, P., Lopez, P., Lupu, C., Radnoti, G., de Rosnay, P., Rozum, I., Vamborg, F., Villaume, S., and Thépaut, J.-N.: The ERA5 global reanalysis, Q. J. Roy. Meteor. Soc., 146, 1999–2049, https://doi.org/10.1002/qj.3803, 2020.

Hochmann, A., Shachar, N., and Gildor, H.: Unraveling sub-seasonal precipitation variability in the Middle East via Indian Ocean sea surface temperatures, Sci. Reports, 14, 2919, https://www.nature.com/articles/s41598-024-53677-x, 2024.

Hochman, A., and Gildor, H.: Synergistic effects of El Niño-Southern Oscillation and the Indian Ocean Dipole on Middle Eastern subseasonal precipitation variability and predictability, Q. J. Roy. Meteor. Soc., 151, 776, https://doi.org/10.1002/qj.4903, 2024.

Hoell, A., Barlow, M., and Saini, R.: The leading pattern of intraseasonal and interannual Indian Ocean precipitation variability and its relationship with Asian circulation during the boreal cold season, J. Climate, 25, 7509–7526, https://doi.org/10.1175/JCLI-D-11-00572.1, 2012.

Hoell, A., Funk, C.: The ENSO-related West Pacific Sea surface temperature gradient, J. Climate, 9545-9562, https://doi.org/10.1175/JCLI-D-12-00344.1, 2013a.

Hoell, A., Barlow, M., and Saini, R.: Intraseasonal and seasonal-to-interannual Indian Ocean convection and hemispheric teleconnections, J. Climate, 26, 8850–8867, https://doi.org/10.1175/JCLI-D-12-00306.1, 2013b.

Hoell, A., Funk, C., and Barlow, M.: The regional forcing of Northern Hemisphere drought during recent warm tropical west Pacific Ocean La Niña events, Clim. Dynam., 42, 3289–3311, https://doi.org/10.1007/s00382-013-1799-4, 2014a.

Hoell, A., Funk, C., and Barlow, M.: La Niña diversity and northwest Indian Ocean Rim teleconnections. Clim. Dynam., 43, 2707–2724, https://doi.org/10.1007/s00382-014-2083-y, 2014b.

Hoell, A., Shukla, S., Barlow, M., Cannon, F., Kelley, C., and Funk, C.: The forcing of monthly precipitation variability over south-west Asia during the boreal cold season, J. Climate, 28, 7038–7056, https://doi.org/10.1175/JCLI-D-14-00757.1, 2015a.

Hoell, A., Funk, C., and Barlow, M.: The Forcing of Southwestern Asia Teleconnections by Low-Frequency Sea Surface Temperature Variability during Boreal Winter, J. Climate, 28, 1511–1526, https://doi.org/10.1175/JCLI-D-14-00344.1, 2015b.

Hoell, A., Barlow, M., Cannon, F., and Xu, T.: Oceanic origins of historical southwest Asia precipitation during the boreal cold season, J. Climate, 30, 2885–2903, https://doi.org/10.1175/JCLID-16-0519.1, 2017.

Hoell, A., Barlow, M., Xu, T., and Zhang, T.: Cold Season Southwest Asia Precipitation Sensitivity to El Niño–Southern Oscillation Events, J. Climate, 31, 4463–4482, https://doi.org/10.1175/JCLI-D-17-0456.1, 2018.

Hoell, A., Robinson, R., Agel, L., Barlow, M. Breeden, M., Eischeid, J., McNally, A., Slinski, K., Quan, X.-W.: Changes to Middle East and Southwest Asia compound drought and heat since 1999, J. Climate, 269-287, https://doi.org/10.1175/JCLI-D-23-0194.1, 2024.

Hoell., A., Breeden, M., Worsnop, R. P., Robinson, R., Agel, L., Anderson, W., Barlow, M., Jayanthi, H., McNally, A., Shukla, S., Slinski K., Verdin, J., Zaheer, F.: An unexpected outcome followed an apparent seasonal forecast of opportunity and prolonged drought in southwest Asia, Int. J. Climatol., 45,8, e8861, https://doi.org/10.1002/joc.8851, 2025.

Hoskins, B. J. and Ambrizzi, T.: Rossby wave propagation on a realistic longitudinally varying flow, J. Atmos. Sci., 50, 12, 1661-1671, https://doi.org/10.1175/1520-0469(1993)050%3C1661:RWPOAR%3E2.0.CO;2, 1993.

Huang, B., Yin, X., Boyer, T., Liu, C., Menne, M., Rao, Y. D., Smith, T., Vose, R., and Zhang, H.: Extended Reconstructed Sea Surface Temperature, Version 6 (ERSSTv6). Part I: An artificial neural network approach, J. Climate, 38, 1105–1121, https://doi.org/10.1175/JCLI-D-23-0707.1, 2025a.

Huang, B., Yin, X., Boyer, T., Liu, C., Menne, M., Rao, Y. D., Smith, T., Vose, R., and Zhang, H.: Extended Reconstructed Sea Surface Temperature, Version 6 (ERSSTv6). Part II: Upgrades on quality control and large-scale filter, J. Climate, 38, 1123–1136, https://doi.org/10.1175/JCLI-D-24-0185.1, 2025b.

Hunt, K. M. R., Baudouin, J.-P., Turner, A. G., Dimri, A. P., Jeelani, G., Pooja, Chattopadhyay, R., Cannon, F., Arulalan, T., Shekhar, M. S., Sabin, T. P., and Palazzi, E.: Western disturbances and climate variability: a review of recent developments, Weather Clim. Dynam., 6, 43–112, https://doi.org/10.5194/wcd-6-43-2025, 2025.

Hussein, K., Alhosani, N., Al-Areeq, A. M., Aghbari, A. A., Elkamali, M., Alsumaiti, T. Sharif, H. O., Almurshidi, A. M. G., and Abdalati, W.: Unprecedented rainfall in the United Arab Emirates: hydrologic and flood impact analysis of the April 2024 event, 121,9363-9385, https://link.springer.com/article/10.1007/s11069-025-07156-9, 2025.

Kadhum, J. H., Al-Zuhairi, M. F., Hashim, A. A.: Synoptic and dynamic analysis of few extreme rainfall events in Iraq, 8, 4939-4952, https://link.springer.com/article/10.1007/s40808-022-01419-1, 2022.

Kahana, R., Ziv, B., Enzel, Y., and Dayan, U.: Synoptic climatology of major floods in the Negev Desert, Israel, Int J. Climatol., 22, 867–882, https://doi.org/10.1002/joc.766, 2002.

Kang, I.-S., Rashid, I. U., Kucharski, F., Almazroui, M., Alkhalaf, A. K.: Multidecadal changes in the relationship between ENSO and wet-season precipitation in the Arabian Peninsula, J. Climate, 28, 4743-4752, https://doi.org/10.1175/JCLI-D-14-00388.1, 2015.

Kelley, C. P., Mohtadi, S., Cane, M. A., Seager, R., and Kushnir, Y.: Climate change in the Fertile Crescent and implications of the recent Syrian drought. Proc. Natl Acad. Sci., 112, 3241–3246, https://doi.org/10.1073/pnas.1421533112, 2015.

Kiladis, G. N., and Diaz, H. F.: Global climatic anomalies associated with extremes in the Southern Oscillation, J. Climate, 2, 1069-1090, https://doi.org/10.1175/1520-0442(1989)002%3C1069:GCAAWE%3E2.0.CO;2, 1989.

Krichak, S. O., Breitgand, J. S., and Feldstein, S. B.: A conceptual model for the identification of the Active Red Sea Trough Synoptic events over the southeastern Mediterranean, J. Appl. Meteor. Climatol., 51, 962–971. https://doi.org/10.1175/JAMC-D-11-0223.1, 2012.

Niranjan Kumar, K., D. Entekhabi, and A. Molini (2015), Hydrological extremes in hyperarid regions: A diagnostic characterization of intense precipitation over the Central Arabian Peninsula, J. Geophys. Res. Atmos., 120, 5, 1637–1650, https://doi.org/10.1002/2014JD022341, 2015.

Kumar, K. N., Ouarda, T. B. M. J., Sandeep, S., and Ajayamohan, R. S.: Wintertime precipitation variability over the Arabian Peninsula and its relationship with ENSO in the CAM4 simulations, Clim. Dyn., 47, 2443-2454, https://link.springer.com/article/10.1007/s00382-016-2973-2, 2016.

Lelieveld, J., Hadjinicolaou, P., Kostopoulou, E., Chenoweth, J., El Maayar, M., Giannakopoulos, C., Hannides, C., Lange, M. A>, Tanarhte, M. Tylris, E., Xoplaki, E.: Climate change and impacts in the Eastern Mediterranean and the Middle East, Climatic Change, 114, 667–687. https://doi.org/10.1007/s10584-012-0418-4, 2012.

Mariotti, A., Ballabrera-Poy, J., and Zeng, N.: Tropical influence on Euro-Asian autumn rainfall variability, 24, 511-521, https://link.springer.com/article/10.1007/s00382-004-0498-6, 2005.

Mariotti, A.: How ENSO impacts precipitation in southwest central Asia, Geophys. Res. Lett., 34, L16706, https://doi.org/10.1029/2007GL030078, 2007.

Matsuno, T.: Quasi-geostrophic motions in the Equatorial Area, J. Meteor., Soc. Japan, 44, 25-43, https://doi.org/10.2151/jmsj1965.44.1_25, 1966.

Middleton, N., and Thomas, D.: World Atlas of desertification, United Nations Environment Programme, Arnold publishers, John Wiley & Sons, Inc., 1997.

Nazemosadat, M. J. and Cordery, I.: On the relationship between ENSO and autumn rainfall in Iran, Int. J. Climatol., 20, 47-61, https://doi.org/10.1002/(SICI)1097-0088(200001)20:1%3C47::AID-JOC461%3E3.0.CO;2-P, 2000.

Nazemosadat, M. J. and Ghasemi, A. R.: Quantifying the ENSO-related shifts in the intensity and probability of drought and wet periods in Iran, J. Climate, 17, 4005–4018, https://doi.org/10.1175/1520-0442(2004)017<4005:QTESIT>2.0.CO;2, 2004.

Nuroozi, H., Shirvanu A., and Barlow, M.: The relationship between moisture in the low level of the troposphere and seasonal precipitation over Iran, Meteorol. Appl., 32, e70033, https://doi.org/10.1002/met.70033, 2025.

Pourasghar, F., Oliver, E. C. J., Holbrook, N. J.: Modulation of wet-season rainfall over Iran by the Madden-Julian Oscillation, Indian Ocean Dipole, and El Niño-Southern Oscillation, Int. J. Climatol., 39, 4029-4040, https://doi.org/10.1002/joc.6057, 2019.

Price, C., Stone, L., Huppert, A., Rajagopalan, B., and Alpert, P.: A possible link between El Nino and precipitation in Israel, Geophys. Res. Lett., 25, 3963–3966, https://doi.org/10.1029/1998GL900098, 1998.

Rezaei, A.: Teleconnections between ocean-atmosphere circulations and historical integrated drought in the Middle East and North Africa, 195, 775, https://link.springer.com/article/10.1007/s10661-023-11386-4, 2023.

Rodwell, M. J. and Hoskins, B. J.: Monsoon and the dynamics of deserts. Quarterly Journal of the Royal Meteorological Society, 122, 1385–1404. https://doi.org/10.1002/qj.49712253408, 1996.

Rodwell, M. J. and Hoskins, B. J.: Subtropical anticyclones and summer monsoons, 14, 3192-3211, https://doi.org/10.1175/1520-0442(2001)014%3C3192:SAASM%3E2.0.CO;2, 2001.

Saji, N. H., Goswami, B. N., Vinayachandran, P. N., and Yamagata, T.: A Dipole Mode in the tropical Indian Ocean, Nature, 401, 360—363, https://doi.org/10.1038/43854, 1999.

Saghafian, B., Haghbegahdar, A., and Dehghani, M. : Effect of ENSO on annual maximum floods and volume over threshold in the southwestern region of Iran, 62, 1039-1049, https://doi.org/10.1080/02626667.2017.1296229, 2017.

Saharwardi, M. S., Dasari, H. P., Aggarwal, V., Ashok, K., and Hoteit, I.: Long-term variability in the Arabian Peninsula droughts driven by the Atlantic Multidecadal Oscillation, Earth's Future, 11, e2023EF003549. https://doi.org/10.1029/2023EF003549, 2024.

Sandeep, S. and Ajayamohan, R. S.: Modulation of winter precipitation dynamics over the Arabian Gulf by ENSO, J. Geophys. Res.-Atmos., 123, 198–210. https://doi.org/10.1002/2017JD027263, 2018.

Schott, F. A., Xie, S.-P., and McCreary Jr., J. P.: Indian Ocean circulation and climate variability, Rev. Geophys., 47, RG1002, https://doi.org/10.1029/2007RG000245, 2009.

Seager, R., Harnik, N., Kushnir, Y., Robinson, W. A., Miller, J.: Mechanisms of hemispherically symmetric Climate variability, J. Climate, 16, 18, 2960-2978, https://doi.org/10.1175/1520-0442(2003)016%3C2960:MOHSCV%3E2.0.CO;2, 2003.

Seager, R., Harnik, N., Robinson, W. A., Kushnir, Y., Ting, M., Huang, H.-P., and Velez, J.: Mechanisms of ENSO-forcing of hemispherically symmetric precipitation variability, Q. J. Roy. Meteor. Soc., 131, 608, 1501-1527, https://doi.org/10.1256/qj.04.96, 2005.

Sohrabi, R.: The politics of drought in the Middle East, case study from Iran, Discover Environ., 3, 122, https://link.springer.com/article/10.1007/s44274-025-00334-3, 2025.

Stuecker, M. F., Timmermann, A., Jin, F.-F., Chikamoto, Y., Zhang, W., Wittenberg, A. T., Widiasih, E., and Zhao, S.: Revisiting ENSO/Indian Ocean Dipole phase relationships, Geophys. Res. Lett., 44, 2481–2492, https://doi.org/10.1002/2016GL072308, 2017.

Tuel, A., Choi, Y.-W., AlRukaibi, D., Eltahir, E. A. B.: Extreme storms in Southwest Asia (Northern Arabian Peninsula) under current and future climate, Clim. Dyn., 58, 1509-1524, https://link.springer.com/article/10.1007/s00382-021-05975-7, 2022.

Tyrlis, E., Lelieveld, J., and Steil, B.: The summer circulation over the eastern Mediterranean and the Middle East: Influence of the South Asian monsoon, Clim. Dyn., 40, 1103–1123, https://doi.org/10.1007/s00382-012-1528-4, 2013.

Wallace, J. M. and Gutzler, D. S.: Teleconnections in the geopotential height field during the Northern Hemisphere winter, Mon. Weather Rev., 109, 784-812, https://doi.org/10.1175/1520-0493(1981)109%3C0784:TITGHF%3E2.0.CO;2, 1981.

Wernli, H. and Sprenger, M.: Identification and ERA-15 climatology of potential vorticity streamers and cutoffs near the extratropical tropopause, J. Atmos. Sci., 64, 1569–1586, https://doi.org/10.1175/JAS3912.1, 2007.

Zittis, G., Almazroui, M., Alpert, P., Ciais, P., Cramer, W., Dahdal, Y., Fnais, M., Francis, D., Hadjinicolaou, P., Howari, F., Jrrar, A., Kaskaoutis, D. G., Kulmala, M., Lazoglou, G., Mihalopoulos, N., Lin, X., Rudich, Y., Sciare, J., Stenchikov, G., Xoplaki, E., and Lelieveld, J.: Climate Change and Weather Extremes in the Eastern Mediterranean and Middle East, Rev. Geophys., 60, e2021RG000762, https://doi.org/10.1029/2021RG000762, 2022.